1
Fundamental Properties of Superconductors

The vanishing of the electrical resistance, the observation of ideal diamagnetism, or the appearance of quantized magnetic flux lines represent characteristic properties of superconductors that we will discuss in detail in this chapter. We will see that all of these properties can be understood, if we associate the superconducting state with a macroscopic coherent matter wave. In this chapter, we will also learn about experiments convincingly demonstrating this wave property. First we turn to the feature providing the name "superconductivity."

1.1
The Vanishing of the Electrical Resistance

The initial observation of the superconductivity of mercury raised a fundamental question about the magnitude of the decrease in resistance on entering the superconducting state. Is it correct to talk about the *vanishing* of the electrical resistance?

During the first investigations of superconductivity, a standard method for measuring electrical resistance was used. The electrical voltage across a sample carrying an electric current was measured. Here, one could only determine that the resistance dropped by more than a factor of a thousand when the superconducting state was entered. One could only talk about the vanishing of the resistance in that the resistance fell below the sensitivity limit of the equipment and, hence, could no longer be detected. Here, we must realize that in principle it is impossible to prove experimentally that the resistance has exactly zero value. Instead, experimentally, we can only find an upper limit of the resistance of a superconductor.

Of course, to understand such a phenomenon, it is highly important to test with the most sensitive methods to see whether a finite residual resistance can also be found in the superconducting state. So we are dealing with the problem of measuring extremely small values of the resistance. Already in 1914 Kamerlingh-Onnes used by far the best technique for this purpose. He detected the decay of an electric current flowing in a closed superconducting ring. If an electrical resistance exists, the stored energy of such a current is transformed gradually into joule heat. Hence, we need to only monitor such a current. If it decays as a function of time, we can be certain that a resistance still exists. If such a decay is observed, one can deduce

Superconductivity: An Introduction, Third Edition. Reinhold Kleiner and Werner Buckel.
© 2016 Wiley-VCH Verlag GmbH & Co. KGaA. Published 2016 by Wiley-VCH Verlag GmbH & Co. KGaA.

COPYRIGHTED MATERIAL

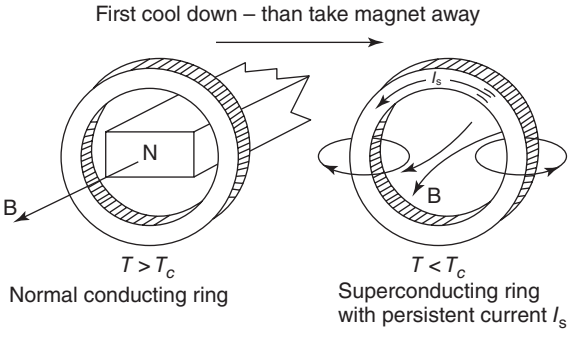

Figure 1.1 The generation of a permanent current in a superconducting ring.

an upper limit of the resistance from the temporal change and from the geometry of the superconducting circuit.

This method is more sensitive by many orders of magnitude than the usual current–voltage measurement. It is shown schematically in Figure 1.1. A ring made from a superconducting material, say, from lead, is held in the normal state above the transition temperature T_c. A magnetic rod serves for applying a magnetic field penetrating the ring opening. Now we cool the ring below the transition temperature T_c at which it becomes superconducting. The magnetic field[1)] penetrating the opening practically remains unchanged. Subsequently we remove the magnet. This induces an electric current in the superconducting ring, since each change of the magnetic flux Φ through the ring causes an electrical voltage along the ring. This induced voltage then generates the current.

If the resistance had exactly zero value, this current would flow without any change as a "permanent current" as long as the lead ring remained superconducting. However, if there exists a finite resistance R, the current would decrease with time, following an exponential decay law. We have

$$I(t) = I_0 \mathrm{e}^{-(R/L)t} \tag{1.1}$$

Here, I_0 denotes the current at some time that we take as time zero; $I(t)$ is the current at time t; R is the resistance; and L is the self-induction coefficient, depending only upon the geometry of the ring.[2)]

1) Throughout we will use the quantity **B** to describe the magnetic field and, for simplicity, refer to it as "magnetic field" instead of "magnetic flux density." Since the magnetic fields of interest (also those within the superconductor) are generated by macroscopic currents only, we do not have to distinguish between the magnetic field **H** and the magnetic flux density **B**, except for a few cases.

2) The self-induction coefficient L can be defined as the proportionality factor between the induction voltage along a conductor and the temporal change of the current passing through the conductor: $U_{\mathrm{ind}} = -L(\mathrm{d}I/\mathrm{d}t)$. The energy stored within a ring carrying a permanent current is given by $(1/2)LI^2$. The temporal change of this energy is exactly equal to the joule heating power RI^2 dissipated within the resistance. Hence, we have $-(\mathrm{d}/\mathrm{d}t)((1/2)LI^2) = RI^2$. One obtains the differential equation $-(\mathrm{d}I/\mathrm{d}t) = (R/L)I$, the solution of which is Eq. (1.1).

For an estimate, we assume that we are dealing with a ring of 5 cm diameter made from a wire with a thickness of 1 mm. The self-induction coefficient L of such a ring is about 1.3×10^{-7} H. If the permanent current in such a ring decreases by less than 1% within an hour, we can conclude that the resistance must be smaller than 4×10^{-13} Ω.[3] This means that in the superconducting state the resistance has changed by more than 8 orders of magnitude.

During such experiments the magnitude of the permanent current must be monitored. Initially [1] this was simply accomplished by means of a magnetic needle, its deflection in the magnetic field of the permanent current being observed. A more sensitive setup was used by Kamerlingh-Onnes and somewhat later by Tuyn [2]. It is shown schematically in Figure 1.2. In both superconducting rings 1 and 2, a permanent current is generated by an induction process. Because of this current both rings are kept in a parallel position. If one of the rings (here the inner one) is suspended from a torsion thread and is slightly turned away from the parallel position, the torsion thread experiences a force originating from the permanent current. As a result, an equilibrium position is established in which the angular moments of the permanent current and of the torsion thread balance each other. This equilibrium position can be observed very sensitively using a light beam. Any decay of the permanent current within the rings would be indicated by the light beam as a change in its equilibrium position. During all such experiments, no change of the permanent current has ever been observed.

A nice demonstration of superconducting permanent currents is shown in Figure 1.3. A small permanent magnet that is lowered toward a superconducting lead bowl generates induction currents according to Lenz's rule, leading to a repulsive force acting on the magnet. The induction currents support the magnet at an equilibrium height. This arrangement is referred to as a *levitated magnet*. The magnet is supported as long as the permanent currents are flowing within the lead bowl, that is, as long as the lead remains superconducting. For high-temperature superconductors such as $YBa_2Cu_3O_7$, the levitation can easily be performed using liquid nitrogen in regular air. Furthermore, it can also serve for levitating freely real heavyweights such as the Sumo wrestler shown in Figure 1.4.

The most sensitive arrangements for determining an upper limit of the resistance in the superconducting state are based on geometries having an extremely small self-induction coefficient L, in addition to an increase in the observation time. In this way, the upper limit can be lowered further. A further increase in the sensitivity is accomplished by the modern superconducting magnetic field sensors (see Section 7.6.4). Today, we know that the jump in resistance during entry into the superconducting state amounts to at least 14 orders of magnitude [3]. Hence, in the superconducting state, a metal can have a specific electrical resistance that

3) For a circular ring of radius r made from a wire of thickness $2d$ also with circular cross-section ($r \gg d$), we have $L = \mu_0 r\,[\ln(8r/d) - 1.75]$ with $\mu_0 = 4\pi \times 10^{-7}$ V s/A m. It follows that

$$R \leq \frac{-\ln 0.99 \times 1.3 \times 10^{-7}}{3.6 \times 10^3} \frac{\text{V s}}{\text{A m}} \cong 3.6 \times 10^{-13}\ \Omega$$

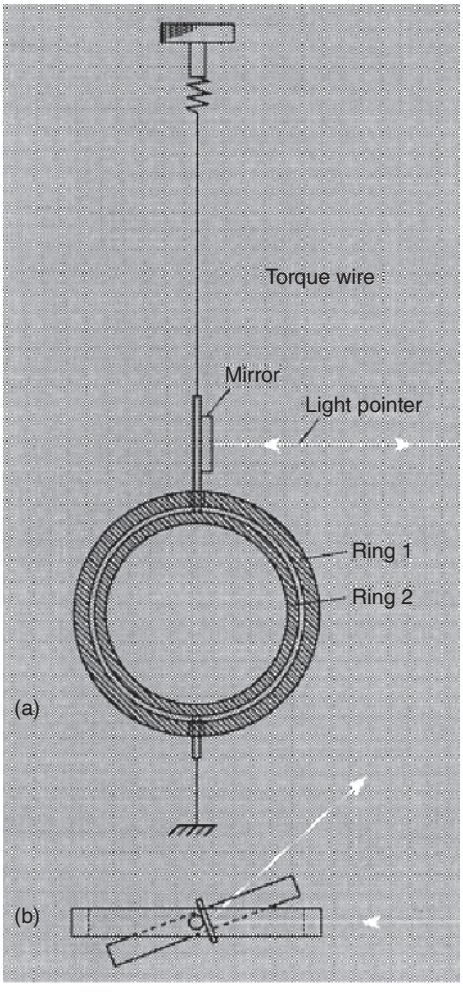

Figure 1.2 Arrangement for the observation of a permanent current. (a) side view, (b) top view. (After [2].) Ring 1 is attached to the cryostat.

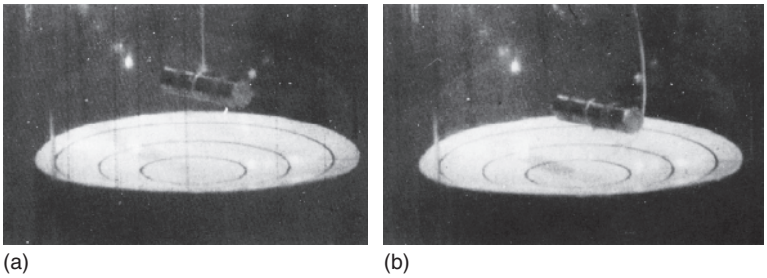

(a) (b)

Figure 1.3 The "levitated magnet" for demonstrating the permanent currents that are generated in superconducting lead by induction during the lowering of the magnet. (a) Starting position. (b) Equilibrium position.

Figure 1.4 Application of free levitation by means of the permanent currents in a superconductor. The Sumo wrestler (including the plate at the bottom) weighs 202 kg. The superconductor is $YBa_2Cu_3O_7$. (Photograph kindly supplied by the International Superconductivity Research Center (ISTEC) and Nihon-SUMO Kyokai, Japan, 1997.)

is at most about 17 orders of magnitude smaller than the specific resistance of copper, one of our best metallic conductors, at 300 K. Since hardly anyone has a clear idea about "17 orders of magnitude," we also present another comparison: the difference in resistance of a metal between the superconducting and normal states is at least as large as that between copper and a standard electrical insulator.

Following this discussion, it appears justified at first to assume that in the superconducting state the electrical resistance actually vanishes. However, we must point out that this statement is valid only under specific conditions. So the resistance can become finite even in the case of small transport currents, if magnetic flux lines exist within the superconductor. Furthermore, alternating currents experience a resistance that is different from zero. We return to this subject in more detail in subsequent chapters.

This totally unexpected behavior of the electric current, flowing without resistance through a metal and at the time contradicting all well-supported concepts, becomes even more surprising if we look more closely at charge transport through a metal. In this way, we can also appreciate more strongly the problem confronting us in terms of an understanding of superconductivity.

We know that electric charge transport in metals takes place through the electrons. The concept that, in a metal, a definite number of electrons per atom (for instance, in the alkalis, one electron, the valence electron) exist freely, rather like a gas, was developed at an early time (by Paul Drude in 1900, and Hendrik Anton Lorentz in 1905). These "free" electrons also mediate the binding of the atoms in metallic crystals. In an applied electric field the free electrons are accelerated. After a specific time, the mean collision time τ, they collide with atoms and lose the energy they have taken up from the electric field. Subsequently, they are accelerated again. The existence of the free charge carriers, interacting with the lattice of the metallic crystal, results in the high electrical conductivity of metals.

Also the increase in the resistance (decrease in the conductivity) with increasing temperature can be understood immediately. With increasing temperature, the uncorrelated thermal motion of the atoms in a metal (each atom is vibrating with a characteristic amplitude about its equilibrium position) becomes more pronounced. Hence, the probability for collisions between the electrons and the atoms increases, that is, the time τ between two collisions becomes smaller. Since the conductivity is directly proportional to this time, in which the electrons are freely accelerated because of the electric field, it decreases with increasing temperature and the resistance increases.

This "free-electron model," according to which electron energy can be delivered to the crystal lattice only due to the collisions with the atomic ions, provides a plausible understanding of electrical resistance. However, within this model, it appears totally inconceivable that, within a very small temperature interval at a finite temperature, these collisions with the atomic ions should abruptly become forbidden. Which mechanism(s) could have the effect that, in the superconducting state, energy exchange between electrons and lattice is not allowed any more? This appears to be an extremely difficult question.

Based on the classical theory of matter, another difficulty appeared with the concept of the free-electron gas in a metal. According to the general rules of classical statistical thermodynamics, each degree of freedom[4)] of a system on average should contribute $k_B T/2$ to the internal energy of the system. Here, $k_B = 1.38 \times 10^{-23}$ W s/K is Boltzmann's constant. This also means that the free electrons are expected to contribute the amount of energy $3k_B T/2$ per free electron, characteristic for a monatomic gas. However, specific heat measurements of metals have shown that the contribution of the electrons to the total energy of metals is about a thousand times smaller than expected from the classical laws.

Here, one can see clearly that the classical treatment of the electrons in metals in terms of a gas of free electrons does not yield a satisfactory understanding. On the other hand, the discovery of energy quantization by Max Planck in 1900 started a totally new understanding of physical processes, particularly on the

4) Each coordinate of a system that appears quadratically in the total energy represents a thermodynamic degree of freedom, for example, the velocity v for $E_{kin} = (1/2)mv^2$, or the displacement x from the equilibrium position for a linear law for the force, $E_{pot} = (1/2)Dx^2$, where D is the force constant.

atomic scale. The following decades then demonstrated the overall importance of quantum theory and of the new concepts resulting from the discovery made by Max Planck. Also the discrepancy between the observed contribution of the free electrons to the internal energy of a metal and the amount expected from the classical theory was resolved by Arnold Sommerfeld in 1928 by means of the quantum theory.

The quantum theory is based on the fundamental idea that each physical system is described in terms of discrete states. A change of physical quantities such as the energy can only take place by a transition of the system from one state to another. This restriction to discrete states becomes particularly clear for atomic objects. In 1913, Niels Bohr proposed the first stable model of an atom, which could explain a large number of facts hitherto not understood. Bohr postulated the existence of discrete stable states of atoms. If an atom in some way interacts with its environment, say, by the gain or loss of energy (e.g., due to the absorption or emission of light), then this is possible only within discrete steps in which the atom changes from one discrete state to another. If the amount of energy (or that of another quantity to be exchanged) required for such a transition is not available, the state remains stable.

In the final analysis, this relative stability of quantum mechanical states also yields the key to the understanding of superconductivity. As we have seen, we need some mechanism(s) forbidding the interaction between the electrons carrying the current in a superconductor and the crystal lattice. If one assumes that the "superconducting" electrons occupy a quantum state, some stability of this state can be understood. Already in about 1930, the concept became accepted that superconductivity represents a typical quantum phenomenon. However, there was still a long way to go for a complete understanding. One difficulty originated from the fact that quantum phenomena were expected for atomic systems, but not for macroscopic objects. In order to characterize this peculiarity of superconductivity, one often referred to it as a *macroscopic quantum phenomenon*. Below we will understand this notation even better.

In modern physics another aspect has also been developed, which must be mentioned at this stage, since it is needed for a satisfactory understanding of some superconducting phenomena. We have learned that the particle picture and the wave picture represent complementary descriptions of one and the same physical object. Here, one can use the simple rule that propagation processes are suitably described in terms of the wave picture and exchange processes during the interaction with other systems in terms of the particle picture.

We illustrate this important point with two examples. Light appears to us as a wave because of many diffraction and interference effects. On the other hand, during the interaction with matter, say, in the photoelectric effect (knocking an electron out of a crystal surface), we clearly notice the particle aspect. One finds that independently of the light intensity the energy transferred to the electron only depends upon the light frequency. However, the latter is expected if light represents a current of particles where all particles have an energy depending on the frequency.

For electrons, we are more used to the particle picture. Electrons can be deflected by means of electric and magnetic fields, and they can be thermally evaporated from metals (glowing cathode). All these are processes where the electrons are described in terms of particles. However, Louis de Broglie proposed the hypothesis that each moving particle also represents a wave, where the wavelength λ is equal to Planck's constant h divided by the magnitude p of the particle momentum, that is, $\lambda = h/p$. The square of the wave amplitude at the location (x, y, z) then is a measure of the probability of finding the particle at this location.

We see that the particle is spatially "smeared" over some distance. If we want to favor a specific location of the particle within the wave picture, we must construct a wave with a pronounced maximum amplitude at this location. Such a wave is referred to as a *wave packet*. The velocity with which the wave packet spatially propagates is equal to the particle velocity.

Subsequently, this hypothesis was brilliantly confirmed. With electrons we can observe diffraction and interference effects. Similar effects also exist for other particles, say, for neutrons. The diffraction of electrons and neutrons has developed into important techniques for structural analysis. In an electron microscope, we generate images by means of electron beams and achieve a spatial resolution much higher than that for visible light because of the much smaller wavelength of the electrons.

For the matter wave associated with the moving particle, there exists, like for each wave process, a characteristic differential equation, the fundamental Schrödinger equation. This deeper insight into the physics of electrons must also be applied to the description of the electrons in a metal. The electrons within a metal also represent waves. Using a few simplifying assumptions, from the Schrödinger equation we can calculate the discrete quantum states of these electron waves in terms of a relation between the allowed energies E and the so-called wave vector $\mathbf{k}$. The magnitude of $\mathbf{k}$ is given by $2\pi/\lambda$, and the spatial direction of $\mathbf{k}$ is the propagation direction of the wave. For a completely free electron, this relation is very simple. We have in this case

$$E = \frac{\hbar^2 \mathbf{k}^2}{2m} \tag{1.2}$$

where m is the electron mass and $\hbar = h/2\pi$.

However, within a metal the electrons are not completely free. First, they are confined to the volume of the piece of metal, like in a box. Therefore, the allowed values of $\mathbf{k}$ are discrete, simply because the allowed electron waves must satisfy specific boundary conditions at the walls of the box. For example, the amplitude of the electron wave may have to vanish at the boundary.

Second, within the metal the electrons experience the electrostatic forces originating from the positively charged atomic ions, in general arranged periodically. This means that the electrons exist within a periodic potential. Near the positively charged atomic ions, the potential energy of the electrons is lower than between these ions. As a result of this periodic potential, in the relation between E and $\mathbf{k}$,

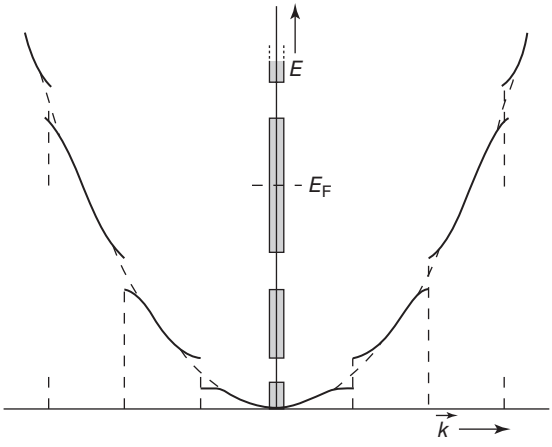

Figure 1.5 Energy–momentum relation for an electron in a periodic potential. The relation (Eq. (1.2)) valid for free electrons is shown as the dashed parabolic line.

not all energies are allowed any more. Instead, there exist different energy ranges separated from each other by ranges with forbidden energies. An example of such an E–$\mathbf{k}$ dependence, modified because of a periodic potential, is shown schematically in Figure 1.5.

So now we are dealing with energy bands. The electrons must be filled into these bands. Here, we have to pay attention to another important principle formulated by Wolfgang Pauli in 1924. This "Pauli principle" requires that in quantum physics each discrete state can be occupied only by a single electron (or more generally by a single particle with a half-integer spin, a so-called "fermion"). Since the angular momentum (spin) of the electrons represents another quantum number with two possible values, according to the Pauli principle each of the discrete $\mathbf{k}$-values can be occupied by only two electrons. In order to accommodate all the electrons of a metal, the states must be filled up to relatively high energies. The maximum energy up to which the states are being filled is referred to as the *Fermi energy* E_F. The density of states per energy interval and per unit volume is referred to simply as the *density of states* $N(E)$. In the simplest case, in momentum space the filled states represent a sphere, the so-called Fermi sphere. However, in general, one finds more complex objects. In a metal the Fermi energy is located within an allowed energy band, that is, the band is only partly filled.[5)] In Figure 1.5, the Fermi energy is indicated for this case.

The occupation of the states is determined by the distribution function for a system of fermions, the Fermi function. This Fermi function takes into account

5) We have an electrical insulator if the accommodation of all the electrons only leads to completely filled bands. The electrons of a filled band cannot take up energy from the electric field, since no free states are available.

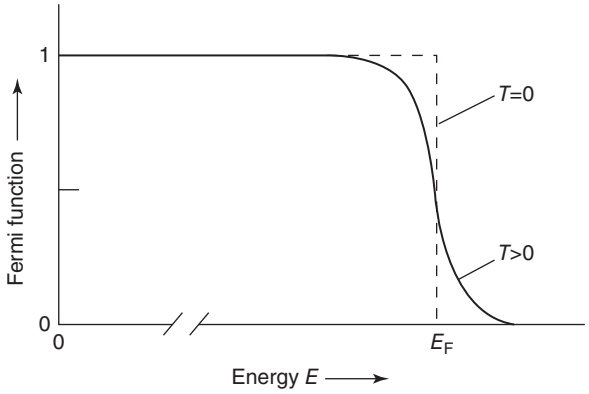

Figure 1.6 Fermi function. E_F is a few electronvolts, whereas thermal smearing is only a few 10^{-3} eV. To indicate this, the abscissa is interrupted.

the Pauli principle and is given by

$$f = \frac{1}{e^{(E-E_F)/k_B T} + 1} \tag{1.3}$$

where k_B is Boltzmann's constant and E_F is the Fermi energy. This Fermi function is shown in Figure 1.6 for the case $T = 0$ (dashed line) and for the case $T > 0$ (solid line). For finite temperatures, the Fermi function is slightly smeared out. This smearing is equal to about the average thermal energy of the fermions. At room temperature, it amounts to about $^1/_{40}$ eV.[6] At finite temperatures, the Fermi energy is the energy at which the distribution function has the value 1/2. In a typical metal, it amounts to about a few electronvolts. This has the important consequence that at normal temperatures the smearing of the Fermi edge is very small. Such an electron system is referred to as a *degenerate electron gas*.

At this stage, we can also understand the very small contribution of the electrons to the internal energy. According to the concepts we have discussed earlier, only very few electrons, namely those within the energy smearing of the Fermi edge, can participate in the thermal energy exchange processes. All other electrons cannot be excited with thermal energies, since they do not find empty states that they could occupy after their excitation.

We have to become familiar with the concept of quantum states and their occupation if we want to understand modern solid-state physics. This is also necessary for an understanding of superconductivity. In order to get used to the many new ideas, we will briefly discuss the mechanism generating electrical resistance. The electrons are described in terms of waves propagating in all directions through the crystal. An electric current results if slightly more waves propagate in one direction than in the opposite direction. The electron waves are scattered because of their interaction with the atomic ions. This scattering corresponds to collisions in the particle picture. What is new in the wave picture

6) eV (electronvolt) is the standard energy unit of elementary processes: $1\,\text{eV} = 1.6 \times 10^{-19}$ W s.

is the fact that this scattering cannot take place for a strongly periodic crystal lattice. The states of the electrons resulting as the solutions of the Schrödinger equation represent stable quantum states. Only a perturbation of the periodic potential, caused by thermal vibrations of the atoms, by defects in the crystal lattice, or by chemical impurities, can lead to a scattering of the electron waves, that is, to a change in the occupation of the quantum states. The scattering due to the thermal vibrations yields a temperature-dependent component of the resistance, whereas that at crystal defects and chemical impurities yields the residual resistance.

After this brief and simplified excursion into the modern theoretical treatment of electronic conduction, we return to our central problem, charge transport with zero resistance in the superconducting state. Also the new wave mechanical ideas do not yet provide an easy access to the appearance of a permanent current. We have only changed the language. Now we must ask: Which mechanisms completely eliminate any energy exchange with the crystal lattice by means of scattering at finite temperatures within a very narrow temperature interval? It turns out that an additional new aspect must be taken into account, namely a particular interaction between the electrons themselves. In our previous discussion we have treated the quantum states of the individual electrons, and we have assumed that these states do not change when they become occupied with electrons. However, if an interaction exists between the electrons, this treatment is no longer correct. Now we must ask instead: What are the states of the system of electrons with an interaction, that is, what collective states exist? Here, we encounter the understanding and also the difficulty of superconductivity. It is a typical collective quantum phenomenon characterized by the formation of a coherent matter wave, propagating through the superconductor without any friction.

1.2
Ideal Diamagnetism, Flux Lines, and Flux Quantization

It has been known for a long time that the characteristic property of the superconducting state is that it shows no measurable resistance for direct current. If a magnetic field is applied to such an *ideal conductor*, permanent currents are generated by induction, which screen the magnetic field from the interior of the sample. In Section 1.1 we have seen this principle already for the levitated magnet.

What happens if a magnetic field $\mathbf{B}_a$ is applied to a *normal conductor* and if subsequently, by cooling below the transition temperature T_c, ideal superconductivity is reached? At first, in the normal state, on application of the magnetic field, eddy currents flow because of induction. However, as soon as the magnetic field reaches its final value and no longer changes with time, these currents decay according to Eq. (1.1), and finally the magnetic fields within and outside the superconductor become equal.

If now the ideal conductor is cooled below T_c, this magnetic state simply remains, since further induction currents are generated only during *changes* of

the field. Exactly this is expected, if the magnetic field is turned off below T_c. In the interior of the ideal conductor, the magnetic field remains conserved.

Hence, depending on the way in which the final state, namely temperature below T_c and applied magnetic field $\mathbf{B}_a$, has been reached, within the interior of the ideal conductor we have completely different magnetic fields.

An experiment by Kamerlingh-Onnes from 1924 appeared to confirm exactly this complicated behavior of a superconductor. Kamerlingh-Onnes [4] cooled a hollow sphere made of lead below the transition temperature in the presence of an applied magnetic field and subsequently turned off the external magnetic field. Then he observed permanent currents and a magnetic moment of the sphere, as expected for the case $R = 0$.

Accordingly, a material with the property $R = 0$, for the same external variables T and $\mathbf{B}_a$, could be transferred into completely different states, depending on the previous history. Therefore, for the same given thermodynamic variables, we would not have just one well-defined superconducting phase, but, instead, a continuous manifold of superconducting phases with arbitrary shielding currents, depending on the previous history. However, the existence of a manifold of superconducting phases appeared so unlikely that, before 1933, one referred to only a single superconducting phase [5] even without experimental verification.

However, a superconductor behaves quite differently from an ideal electrical conductor. Again, we imagine that a sample is cooled below T_c in the presence of an applied magnetic field. If this magnetic field is very small, one finds that the field is completely expelled from the interior of the superconductor except for a very thin layer at the sample surface. In this way, one obtains an ideal diamagnetic state, independent of the temporal sequence in which the magnetic field was applied and the sample was cooled.

This ideal diamagnetism was discovered in 1933 by Meissner and Ochsenfeld for rods made of lead or tin [6]. This expulsion effect, similar to the property $R = 0$, can be nicely demonstrated using the "levitated magnet."[7] In order to show the property $R = 0$, in Figure 1.3 we have lowered the permanent magnet toward the superconducting lead bowl, in this way generating permanent currents by induction. To demonstrate the Meissner–Ochsenfeld effect, we place the permanent magnet into the lead bowl at $T > T_c$ (Figure 1.7a) and then cool down further. The field expulsion appears at the superconducting transition: the magnet is repelled from the diamagnetic superconductor, and it is raised up to the equilibrium height (Figure 1.7b). In the limit of ideal magnetic field expulsion, the same levitation height is reached as in Figure 1.3.

What went wrong during the original experiment of Kamerlingh-Onnes? He used a hollow sphere in order to consume a smaller amount of liquid helium for cooling. The observations for this sample were correct. However, he had overlooked the fact that during cooling of a hollow sphere a closed ring-shaped superconducting object can be formed, which keeps the magnetic flux penetrating its

7) Also non-superconducting, but diamagnetic objects, such as nuts or frogs, can levitate above magnets. However, one needs very large field gradients [7].

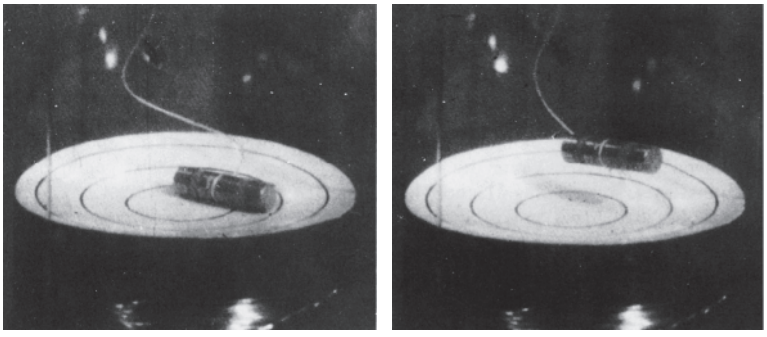

Figure 1.7 "Levitated magnet" for demonstrating the Meissner–Ochsenfeld effect in the presence of an applied magnetic field. (a) Starting position at $T > T_c$. (b) Equilibrium position at $T < T_c$.

open area constant. Hence, a hollow sphere can act like a superconducting ring (Figure 1.1), leading to the observed result.

Above, we had assumed that the magnetic field applied to the superconductor would be "small." Indeed, one finds that ideal diamagnetism only exists within a finite range of magnetic fields and temperatures, which, furthermore, also depends on the sample geometry.

Next, we consider a long, rod-shaped sample where the magnetic field is applied parallel to the axis. For other shapes, the magnetic field can often be distorted. For an ideal diamagnetic sphere, at the "equator" the magnetic field is 1.5 times larger than the externally applied field. In Section 4.6.4, we will discuss these geometric effects in more detail.

One finds that there exist two different types of superconductors:

- The first type, referred to as *type-I superconductors* or *superconductors of the first kind*, expels the magnetic field up to a maximum value B_c, the critical field. For larger fields, superconductivity breaks down, and the sample assumes the normal conducting state. Here, the critical field depends on the temperature and reaches zero at the transition temperature T_c. Mercury and lead are examples of a type-I superconductor.
- The second type, referred to as *type-II superconductors* or *superconductors of the second kind*, shows ideal diamagnetism for magnetic fields smaller than the "lower critical magnetic field" B_{c1}. Superconductivity completely vanishes for magnetic fields larger than the "upper critical magnetic field" B_{c2}, which often is much larger than B_{c1}. Both critical fields reach zero at T_c. This behavior is found in many alloys and also in the high-temperature superconductors. In the latter, B_{c2} can reach even values larger than 100 T.

What happens in type-II superconductors in the "Shubnikov phase" between B_{c1} and B_{c2}? In this regime, the magnetic field only partly penetrates into the sample. Now shielding currents flow within the superconductor and concentrate the magnetic field lines, such that a system of flux lines, also referred to as *Abrikosov*

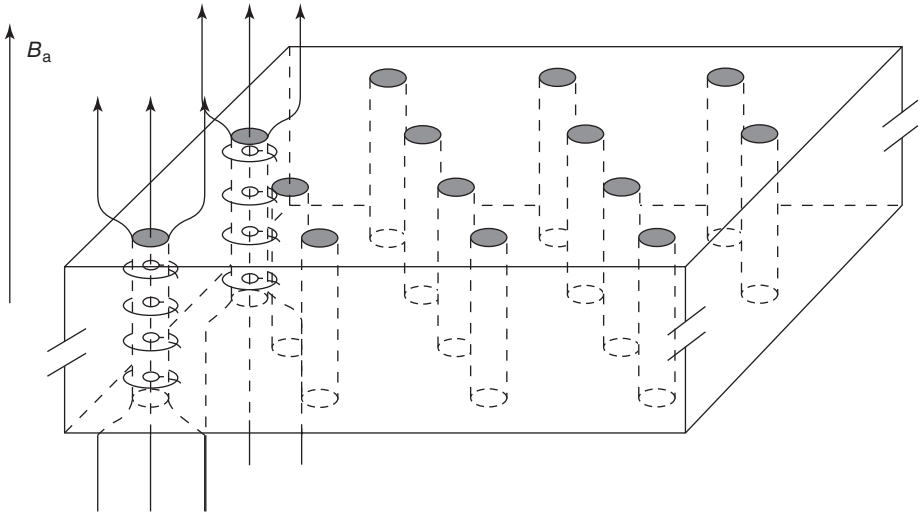

Figure 1.8 Schematic diagram of the Shubnikov phase. The magnetic field and the supercurrents are shown only for two flux lines.

vortices, is generated. For the prediction of quantized flux lines, A. A. Abrikosov received the Nobel Prize in physics in 2003. In an ideal homogeneous superconductor in general, these vortices arrange themselves in the form of a triangular lattice. In Figure 1.8 we show schematically this structure of the Shubnikov phase. The superconductor is penetrated by magnetic flux lines, each of which carries a magnetic flux quantum and is located at the corners of equilateral triangles. Each flux line consists of a system of circulating currents, which in Figure 1.8 are indicated for two flux lines. These currents together with the external magnetic field generate the magnetic flux within the flux line and reduce the magnetic field between the flux lines. Hence, one also talks about flux vortices. With increasing external field $\mathbf{B}_a$, the distance between the flux lines becomes smaller.

The first experimental proof of a periodic structure of the magnetic field in the Shubnikov phase was given in 1964 by a group at the Nuclear Research Center in Saclay using neutron diffraction [8]. However, they could only observe a basic period of the structure. Beautiful neutron diffraction experiments with this magnetic structure were performed by a group at the Nuclear Research Center, Jülich [9]. Real images of the Shubnikov phase were generated by Essmann and Träuble [10] using an ingenious decoration technique. In Figure 1.9, we show a lead–indium alloy as an example. These images of the magnetic flux structure were obtained as follows: Above the superconducting sample, iron atoms are evaporated from a hot wire. During their diffusion through the helium gas in the cryostat, the iron atoms coagulate to form iron colloids. These colloids have a diameter of less than 50 nm, and they slowly approach the surface of the superconductor. At this surface, the flux lines of the Shubnikov phase exit from the superconductor. In Figure 1.8, this is shown for two flux lines. The ferromagnetic iron colloid is collected at the locations where the flux lines exit from the surface, since here they

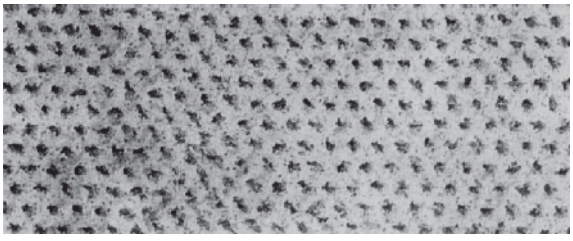

Figure 1.9 Image of the vortex lattice obtained with an electron microscope following the decoration with iron colloid. Frozen-in flux after the magnetic field has been reduced to zero. Material: Pb +6.3 at% In; temperature: 1.2 K; sample shape: cylinder, 60 mm long, 4 mm diameter; and magnetic field $\mathbf{B}_a$ parallel to the axis. Magnification: 8300×. (Reproduced by courtesy of Dr Essmann.)

find the largest magnetic field gradients. In this way, the flux lines can be decorated. Subsequently, the structure can be observed in an electron microscope. The image shown in Figure 1.9 was obtained in this way. Such experiments convincingly confirmed the vortex structure predicted theoretically by Abrikosov.

The question remains whether the decorated locations at the surface indeed correspond to the ends of the flux lines carrying only a single flux quantum. In order to answer this question, we just have to count the number of flux lines and also have to determine the total flux, say, by means of an induction experiment. Then we find the value of the magnetic flux of a flux line by dividing the total flux Φ_{tot} through the sample by the number of flux lines. Such evaluations exactly confirmed that in highly homogeneous type-II superconductors, each flux line contains a single flux quantum $\Phi_0 = 2.07 \times 10^{-15}$ T m^2.

Today, we know different methods for imaging magnetic flux lines. Often, the methods supplement each other and provide valuable information about superconductivity. Therefore, we will discuss some of them in more detail.

Neutron diffraction and decoration still represent important techniques. Figure 1.10a shows a diffraction pattern observed at the Institute Laue-Langevin in Grenoble by means of neutron diffraction at the vortex lattice in niobium. The triangular structure of the vortex lattice can clearly be seen from the diffraction pattern.

Magneto-optics represents another method for spatially imaging magnetic structures. Here, one utilizes the Faraday effect. If linearly polarized light passes through a thin layer of a "Faraday-active" material such as a ferrimagnetic garnet film, the plane of polarization of the light will be rotated due to a magnetic field within the garnet film. A transparent substrate, covered with a thin ferrimagnetic garnet film, is placed on top of a superconducting sample and is irradiated with polarized and well-focused light. The light is reflected at the superconductor, passes through the ferrimagnetic garnet film again, and is then focused into a CCD camera. The magnetic field from the vortices in the superconductor penetrates into the ferrimagnetic garnet film and there causes a rotation of the plane of polarization of the light. An analyzer located in front of the CCD camera only transmits light whose polarization is rotated away from the original direction.

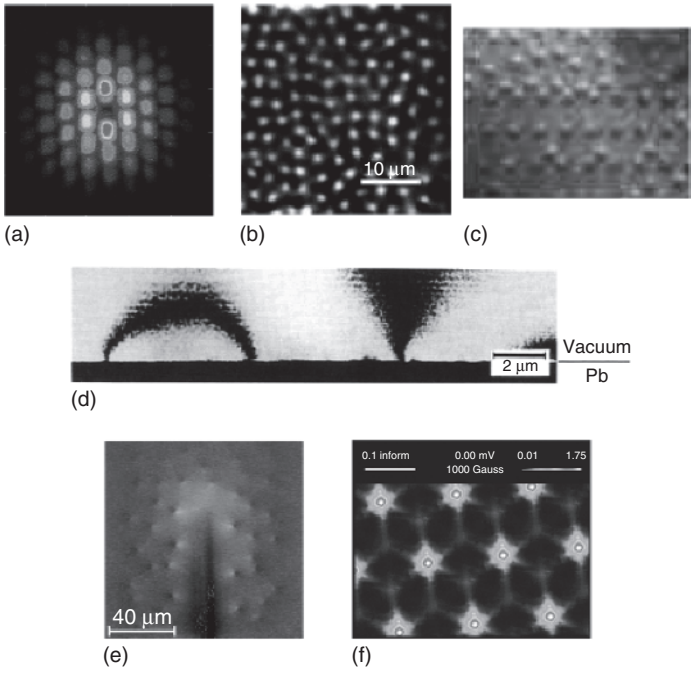

Figure 1.10 Methods for the imaging of flux lines. (a) Neutron diffraction pattern of the vortex lattice in niobium (Figure kindly provided by Institute Max von Laue-Paul Langevin, Grenoble; Authors: E. M. Forgan (Univ. Birmingham), S. L. Lee (Univ. St. Andrews), D. McK.Paul (Univ. Warwick), H. A. Mook (Oak Ridge) and R. Cubitt (ILL).). (b) Magneto-optical image of vortices in $NbSe_2$ [11]. (c) Lorentz microscopy of niobium (Figure kindly provided by A. Tonomura, Fa. Hitachi Ltd.). (d) Electron holography of Pb [12]. (e) Low-temperature scanning electron microscopy of $YBa_2Cu_3O_7$ [13]. (f) Scanning tunneling microscopy of $NbSe_2$ (Figure kindly provided by Fa. Lucent Technologies Inc./Bell labs).

In this way, the vortices appear as bright dots, as shown in Figure 1.10b for the compound $NbSe_2$ [11].[8] This method yields a spatial resolution of more than 1 µm. Presently, one can take about 10 images/s, also allowing the observation of dynamic processes. Unfortunately, at this time, the method is restricted to superconductors with a very smooth and highly reflecting surface.

For Lorentz microscopy, an electron beam is transmitted through a thin superconducting sample. The samples must be very thin, and the electron energy must be high in order that the beam penetrates through the sample. Near a flux line the transmitted electrons experience an additional Lorentz force, and the electron beam is slightly defocused due to the magnetic field gradient of a flux line. The phase contrast caused by the flux lines can be imaged beyond the focus of the

8) We note that in this case the vortex lattice is strongly distorted. Such distorted lattices will be discussed in more detail in Section 5.3.2.

transmission electron microscope. Because of the deflection, each vortex appears as a circular signal: one half of which is bright, and the other half is dark. This alternation between bright and dark also yields the polarity of the vortex. Lorentz microscopy allows a very rapid imaging of the vortices, such that motion pictures can be taken, clearly showing the vortex motion, similar to the situation for magneto-optics [14]. Figure 1.10c shows such an image obtained for niobium by A. Tonomura (Hitachi Ltd). This sample carried small micro-holes (antidots) arranged as a square lattice. In the image, most of the micro-holes are occupied by vortices, and some vortices are located between the antidots. The vortices enter the sample from the top side. Then they are hindered from further penetration into the sample by the antidots and by the vortices already existing in the superconductor.

Electron holography [14] is based on the wave nature of electrons. Similar to optical holography, a coherent electron beam is split into a reference wave and an object wave, which subsequently interfere with each other. The relative phase position of the two waves can be influenced by a magnetic field, or more accurately by the magnetic flux enclosed by both waves. The effect utilized for imaging is closely related to the magnetic flux quantization in superconductors. In Section 1.5.2, we will discuss this effect in more detail. In Figure 1.10d, the magnetic stray field generated by vortices near the surface of a lead film is shown [12]. The alternation from bright to dark in the interference stripes corresponds to the magnetic flux of one flux quantum. On the left side the magnetic stray field between two vortices of opposite polarity joins together, whereas on the right side the stray field turns away from the superconductor.

For imaging by means of low-temperature scanning electron microscopy (LTSEM), an electron beam is scanned along the surface of the sample to be studied. As a result, the sample is heated locally by a few kelvin within a spot of about 1 μm diameter. An electronic property of the superconductor, which changes due to this local heating, is then measured. With this method, many superconducting properties, such as, the transition temperature T_c, can be spatially imaged [15]. In the special case of the imaging of vortices, the magnetic field of the vortex is detected using a superconducting quantum interferometer (or superconducting quantum interference device, "SQUID," see Section 1.5.2) [13]. If the electron beam passes close to a vortex, the supercurrents flowing around the vortex axis are distorted, resulting in a small displacement of the vortex axis toward the electron beam. This displacement also changes the magnetic field of the vortex detected by the quantum interferometer, and this magnetic field change yields the signal to be imaged. A typical image of vortices in the high-temperature superconductor $YBa_2Cu_3O_7$ is shown in Figure 1.10e. Here, the vortices are located within the quantum interferometer itself. Similar to Lorentz microscopy, each vortex is indicated as a circular bright/dark signal, generated by the displacement of the vortex in different directions. The dark vertical line in the center indicates a slit in the quantum interferometer, representing the proper sensitive part of the magnetic field sensor. We note the highly irregular arrangement of the vortices. A specific advantage of this

technique is the fact that very small displacements of the vortices from their equilibrium position can also be observed, since the SQUID already detects a change of the magnetic flux of only a few millionths of a magnetic flux quantum. Such changes occur, for example, if the vortices statistically jump back and forth between two positions due to thermal motion. Since such processes can strongly reduce the resolution of SQUIDs, they are being carefully investigated using LTSEM.

As the last group of imaging methods, we wish to discuss the scanning probe techniques, in which a suitable detector is moved along the superconductor. The detector can be a magnetic tip [16], a micro-Hall probe [17], or a SQUID [18]. In particular, the latter method has been used in a series of key experiments for clarifying our understanding of high-temperature superconductors. These experiments will be discussed in Section 3.2.2. Finally, the scanning tunneling microscope yielded similarly important results. Here, a non-magnetic metallic tip is scanned along the sample surface. The distance between the tip and the sample surface is so small that electrons can flow from the sample surface to the tip because of the quantum mechanical tunneling process.

Contrary to the methods mentioned earlier, (all of which detect the magnetic field of vortices), with the scanning tunneling microscope one images the spatial distribution of the electrons, or more exactly of the density of the allowed quantum mechanical states of the electrons [19]. This technique can reach atomic resolution. In Figure 1.10f we show an example. This image was obtained by H. F. Hess and coworkers (Bell Laboratories, Lucent Technologies Inc.) using an $NbSe_2$ single crystal. The applied magnetic field was $1000\,G = 0.1\,T$. Later, we will discuss the fact that, near the vortex axis, the superconductor is normal conducting. It is this region where the tunneling currents between the tip and the sample reach their maximum values. Hence, the vortex axis appears as a bright spot.

In addition to the imaging methods, there exists a series of other techniques for characterizing the vortex state. In the case of muon-spin-resonance (μSR), the superconductor is irradiated with spin-polarized, usually positively charged muons, which are generated by a particle accelerator. The muons are rapidly stopped within the superconductor. In the local magnetic fields, the spin of the muon precesses. After about 2 μs, the muon decays into two neutrinos and one positron. During the decay, the positron is emitted along the direction of the muon spin. Hence, its detection yields information about the local magnetic fields in the interior of the superconductor and thereby also about the structure of the flux-line lattice. Other indirect methods are based, for example, on the analysis of the specific heat or of transport phenomena such as the thermal conductivity or the electric conductivity, which becomes finite at sufficiently large currents (see Chapter 5).

Finally, we note that a superconductor can also levitate in the state of the Shubnikov phase. The superconductor $YBa_2Cu_3O_7$ shown in Figure 1.4 had been cooled in the field of the permanent magnets and was penetrated by magnetic flux lines. It

is essential that the flux lines can be pinned at defects within the superconductor. The corresponding physics will be discussed in Section 5.3.2.

In the case of the "hard" superconductors, this pinning phenomenon is particularly effective. If they are pinned, the flux lines cannot move as long as the maximum pinning force of the pinning centers is not exceeded. As a result, the hard superconductor will keep the field in its interior at the value at which it had been cooled down.

If the superconductor is cooled down at a certain distance above a permanent magnet, an *attractive* force is acting if one tries to move the superconductor away from the magnet. Similarly, a *repulsive* force is generated if the superconductor is moved closer to the permanent magnet. In the end, the hard superconductor tries to keep exactly the distance to the magnet in which it was cooled down. The same applies to any other motional direction. As soon as the external field changes, shielding currents are generated in the hard superconductor in such a way that the field (and the flux-line lattice) in its interior does not change. Therefore, a hard superconductor including a heavy load can not only levitate above a magnet as shown in Figure 1.4, but it can also hang freely below a magnet, or it can be positioned at an arbitrary angle. This effect is demonstrated in Figure 1.11. In this case suitably prepared small blocks made of $YBa_2Cu_3O_7$ were mounted within a toy train, and the blocks were cooled down at a certain distance from the magnets, which represented the "train tracks." The train can move along the tracks practically without friction, since the magnetic field remains constant along this direction.

With this toy train a special trick was demonstrated, which keeps the hanging train from falling down after heating above T_c. Permanent magnets were installed in the train in such a way that in the absence of the superconductor the train would be pulled to the track. This happens exactly, if the superconductor heats up. However, in the superconducting state, against the attraction by the

Figure 1.11 Hanging toy train [20] (Leibniz Institute for Solid State and Materials Research, Dresden).

permanent magnets the train is kept away from the track and can move freely along it.

1.3 Flux Quantization in a Superconducting Ring

Again we look at the experiment shown in Figure 1.1. A permanent current has been generated in a superconducting ring by induction. How large is the magnetic flux through the ring?

The flux is given by the product of the self-inductance L of the ring and the current I circulating in the ring: $\Phi = LI$. From our experience with macroscopic systems, we would expect that we could generate by induction any value of the permanent current by the proper choice of the magnetic field. Then also the magnetic flux through the ring could take any arbitrary value. On the other hand, we have seen that in the interior of type-II superconductors magnetic fields are concentrated in the form of flux lines, each of which carries a single flux quantum Φ_0. Now the question arises whether the flux quantum also plays a role in a superconducting ring. Already in 1950 such a presumption was expressed by Fritz London [21].

In 1961, two groups, namely Doll and Näbauer [22] in Munich and Deaver and Fairbank [23] in Stanford, published the results of flux quantization measurements using superconducting hollow cylinders, which clearly showed that the magnetic flux through the cylinder only appears in multiples of the flux quantum Φ_0. These experiments had a strong impact on the development of superconductivity. Because of their importance and their experimental excellence, we will discuss these experiments in more detail.

For testing the possible existence of flux quantization in a superconducting ring or hollow cylinder, permanent currents had to be generated using different magnetic fields, and the resulting magnetic flux had to be determined with a resolution of better than a flux quantum Φ_0. Due to the small value of the flux quantum, such experiments are extremely difficult. To achieve a relatively large change of the magnetic flux in different states, one must try to keep the flux through the ring in the order of only a few Φ_0. Hence, one needs very small superconducting rings, since otherwise the magnetic fields required to generate the permanent currents become too small. We refer to these fields as "freezing fields," since the generated flux through the opening of the ring is "frozen-in" during the onset of superconductivity. For example, in an opening of only 1 mm^2, one flux quantum already exists in a field of only 2×10^{-9} T.

Therefore, both groups used very small samples in the form of thin tubes with a diameter of only about 10 µm. For this diameter, one flux quantum $\Phi_0 = h/2e = 2.07 \times 10^{-15}$ T m^2 is generated in a field of only $\Phi_0/\pi r^2 = 2.6 \times 10^{-5}$ T. With careful shielding of perturbing magnetic fields, for example, of the Earth's magnetic field, such fields can be well controlled experimentally.

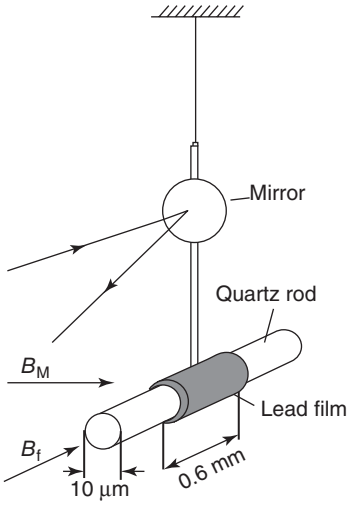

Figure 1.12 Schematics of the experimental setup of Doll and Näbauer. (From [22].) The quartz rod carries a small lead cylinder formed as a thin layer by evaporation. The rod vibrates in liquid helium.

Doll and Näbauer utilized lead cylinders evaporated onto little quartz rods (Figure 1.12). Within these lead cylinders, a permanent current is generated by cooling in a freezing field B_f oriented parallel to the cylinder axis and by turning off this field after the onset of superconductivity at $T < T_c$. The permanent current turns the lead cylinder into a magnet. In principle, the magnitude of the frozen-in flux can be determined from the torque exerted upon the sample due to the measuring field B_M oriented perpendicular to the cylinder axis. Therefore, the sample is attached to a quartz thread. The deflection can be indicated by means of a light beam and a mirror. However, the attained torque values were too small to be detected in a static experiment using extremely thin quartz threads. Doll and Näbauer circumvented this difficulty using an elegant technique, which may be called a *self-resonance method*.

They utilized the small torque exerted upon the lead cylinder by the measuring field to excite a torsional oscillation of the system. At resonance, the amplitudes become sufficiently large that they can be recorded without difficulty. At resonance, the amplitude is proportional to the acting torque to be measured. For the excitation, the magnetic field B_M must be reversed periodically at the frequency of the oscillation. To ensure that the excitation always follows the resonance frequency, the reversal of the field was controlled by the oscillating system itself using the light beam and a photocell.

In Figure 1.13 we show the results of Doll and Näbauer. On the ordinate the resonance amplitude is plotted, divided by the measuring field, that is, a quantity proportional to the torque to be determined. The abscissa indicates the freezing field. If the flux in the superconducting lead cylinder varied continuously, the observed resonance amplitude also should vary proportional to the freezing field (dashed straight line in Figure 1.13). The experiment clearly indicates a different behavior. Up to a freezing field of about 1×10^{-5} T, no flux at all is frozen-in.

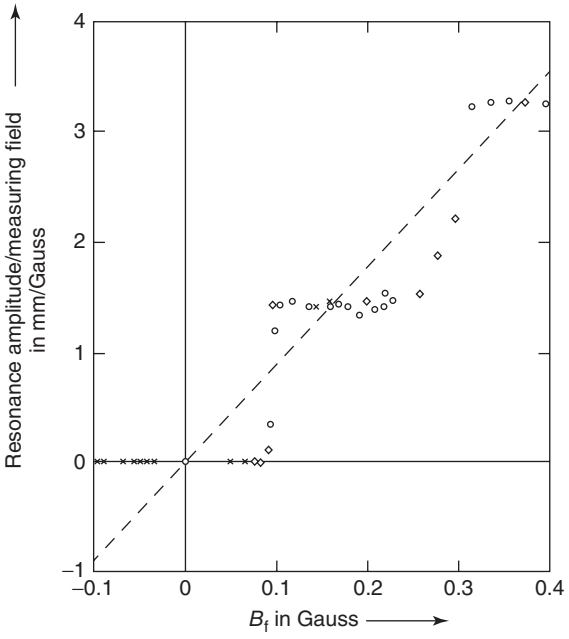

Figure 1.13 Results of Doll and Näbauer on the magnetic flux quantization in a Pb cylinder ($1\,G = 10^{-4}$ T). .(From [22].)

The superconducting lead cylinder remains in the energetically lowest state with $\Phi = 0$. Only for freezing fields larger than 1×10^{-5} T does a state appear containing frozen-in flux. For all freezing fields between 1×10^{-5} and about 3×10^{-5} T, the state remains the same. In this range, the resonance amplitude is constant. The flux calculated from this amplitude and from the parameters of the apparatus corresponds approximately to a flux quantum $\Phi_0 = h/2e$. For larger freezing fields, additional quantum steps are observed. This experiment clearly demonstrates that the magnetic flux through a superconducting ring can take up only discrete values $\Phi = n\Phi_0$.

An example of the results of Deaver and Fairbank is shown in Figure 1.14. Their results also demonstrated the quantization of magnetic flux through a superconducting hollow cylinder and confirmed the elementary flux quantum $\Phi_0 = h/2e$. Deaver and Fairbank used a completely different method for detecting the frozen-in flux. They moved the superconducting cylinder back and forth by 1 mm along its axis at a frequency of 100 Hz. As a result, in two small detector coils surrounding the two ends of the little cylinder, respectively, an inductive voltage was generated, which could be measured after sufficient amplification. In Figure 1.14 the flux through the little tube is plotted in multiples of the elementary flux quantum Φ_0 versus the freezing field. The states with 0, 1, and 2 flux quanta can clearly be seen.

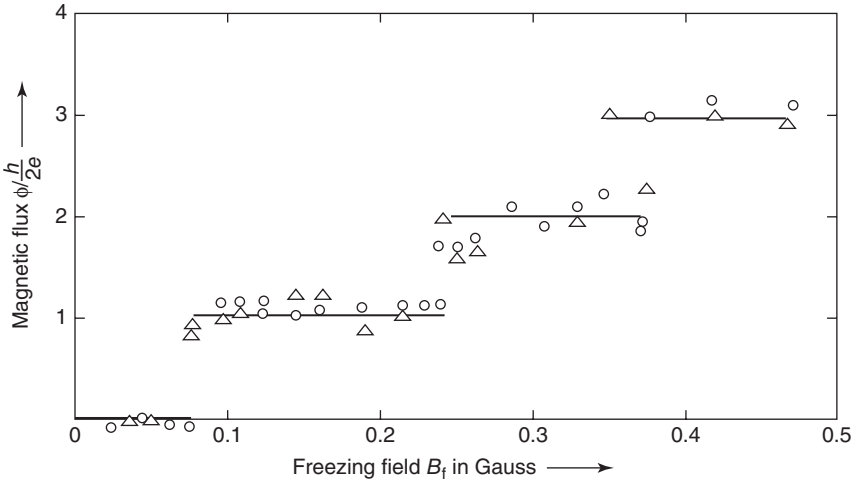

Figure 1.14 Results of Deaver and Fairbank on the magnetic flux quantization in a Sn cylinder. The cylinder was about 0.9 mm long, and had an inner diameter of 13 μm and a wall thickness of 1.5 μm ($1\,G = 10^{-4}\,T$). (From [23].)

1.4 Superconductivity: A Macroscopic Quantum Phenomenon

Next, we will deal with the conclusions to be drawn from the quantization of the magnetic flux in units of the flux quantum Φ_0.

For atoms we are well used to the appearance of discrete states. For example, the stationary atomic states are distinguished due to a quantum condition for the angular momentum appearing in multiples of $\hbar = h/2\pi$. This quantization of the angular momentum is a result of the condition that the quantum mechanical wave function, indicating the probability of finding the electron, be single-valued. If we move around the atomic nucleus starting from a specific point, the wave function must reproduce itself exactly if we return to this starting point. Here, the phase of the wave function can change by an integer multiple of 2π, since this does not affect the wave function.

We can have the same situation also on a macroscopic scale. Imagine that we have an arbitrary wave propagating without damping in a ring with radius R. The wave can become stationary if an integer number n of wavelengths λ exactly fit into the ring. Then we have the condition $n\lambda = 2\pi R$ or $kR = n$, using the wavenumber $k = 2\pi/\lambda$. If this condition is violated, after a few revolutions the wave disappears due to interference.

Next we apply these ideas to an electron wave propagating around the ring. For an exact treatment, we would have to solve the Schrödinger equation for the relevant geometry. However, we refrain from this and, instead, we restrict ourselves to a semiclassical treatment, also yielding the essential results.

We start with the relation between the wave vector of the electron and its momentum. According to de Broglie, for an uncharged quantum particle we have $\mathbf{p}_{\text{kin}} = \hbar\mathbf{k}$, where $\mathbf{p}_{\text{kin}} = m\mathbf{v}$ denotes the "kinetic momentum" (where m is the mass and $\mathbf{v}$ is the velocity of the particle). This yields the kinetic energy of the particle: $E_{\text{kin}} = (\mathbf{p}_{\text{kin}})^2/2m$. For a charged particle as the electron, according to the rules of quantum mechanics, the wave vector $\mathbf{k}$ depends on the so-called vector potential $\mathbf{A}$. This vector potential is connected with the magnetic field through the relation[9)]

$$\operatorname{curl}\mathbf{A} = \mathbf{B} \tag{1.4}$$

We define the "canonical momentum"

$$\mathbf{p}_{\text{can}} = m\mathbf{v} + q\mathbf{A} \tag{1.5}$$

where m is the mass and q is the charge of the particle. Then the relation between the wave vector $\mathbf{k}$ and $\mathbf{p}_{\text{can}}$ is

$$\mathbf{p}_{\text{can}} = \hbar\mathbf{k} \tag{1.6}$$

Now we require that an integer number of wavelengths exists within the ring. We integrate $\mathbf{k}$ along an integration path around the ring, and we set this integral equal to an integer multiple of 2π. Then we have

$$n{\cdot}2\pi = \oint \mathbf{k}\,\mathrm{d}\mathbf{r} = \frac{1}{\hbar}\oint \mathbf{p}_{\text{can}}\,\mathrm{d}\mathbf{r} = \frac{m}{\hbar}\oint \mathbf{v}\,\mathrm{d}\mathbf{r} + \frac{q}{\hbar}\oint \mathbf{A}\,\mathrm{d}\mathbf{r} \tag{1.7}$$

According to Stokes' theorem, the second integral ($\oint \mathbf{A}\,\mathrm{d}\mathbf{r}$) on the right-hand side can be replaced by the area integral $\int_F \operatorname{curl}\mathbf{A}\,\mathrm{d}\mathbf{f}$ taken over the area F enclosed by the ring. However, this integral is nothing other than the magnetic flux $\int_F \operatorname{curl}\mathbf{A}\,\mathrm{d}\mathbf{f} = \int_F \mathbf{B}\,\mathrm{d}\mathbf{f} = \Phi$ enclosed by the ring. Hence, Eq. (1.7) can be changed into

$$n\frac{h}{q} = \frac{m}{q}\oint \mathbf{v}\,\mathrm{d}\mathbf{r} + \Phi \tag{1.8}$$

Here, we have multiplied Eq. (1.7) by $\hbar/q$ and used $\hbar = h/2\pi$.

In this way, we have found a quantum condition connecting the magnetic flux through the ring with Planck's constant and the charge of the particle. If the path integral on the right-hand side of Eq. (1.8) is constant, the magnetic flux through the ring changes exactly by a multiple of h/q.

So far we have discussed only a single particle. However, what happens if all or at least many charge carriers occupy the same quantum state? Also in this case, we can describe these charge carriers in terms of a single coherent matter wave with

9) The "curl" of a vector $\mathbf{A}$ is again a vector, the components $(\operatorname{curl}\mathbf{A})_x$, … of which are constructed from the components A_i in the following way:

$$(\operatorname{curl}\mathbf{A})_x = \frac{\partial A_z}{\partial y} - \frac{\partial A_y}{\partial z}; \quad (\operatorname{curl}\mathbf{A})_y = \frac{\partial A_x}{\partial z} - \frac{\partial A_z}{\partial x}, \quad (\operatorname{curl}\mathbf{A})_z = \frac{\partial A_y}{\partial x} - \frac{\partial A_x}{\partial y}.$$

a well-defined phase, and where all charge carriers jointly change their quantum states. In this case, Eq. (1.8) is also valid for this coherent matter wave.

However, now we are confronted with the problem that electrons must satisfy the Pauli principle and must occupy different quantum states, like all quantum particles having half-integer spin. Here, the solution comes from the pairing of two electrons, forming Cooper pairs in an ingenious way. In Chapter 3, we will discuss this pairing process in more detail. Then each pair has an integer spin that is equal to zero for most superconductors. The coherent matter wave can be constructed from these pairs. The wave is connected with the motion of the center of mass of the pairs, which is identical for all pairs.

Next, we will further discuss Eq. (1.8) and see what conclusions can be drawn regarding the superconducting state. We start by connecting the velocity $\mathbf{v}$ with the supercurrent density $\mathbf{j}_s$ via $\mathbf{j}_s = qn_s\mathbf{v}$. Here, n_s denotes the density of the superconducting charge carriers. For generality, we keep the notation q for the charge. Now Eq. (1.8) can be rewritten as

$$n\frac{h}{q} = \frac{m}{q^2 n_s}\oint \mathbf{j}_s \, \mathrm{d}\mathbf{r} + \Phi \tag{1.9}$$

Furthermore, we introduce the abbreviation $m/(q^2 n_s) = \mu_0 \lambda_L^2$. The length

$$\lambda_L = \sqrt{m/(\mu_0 q^2 n_s)} \tag{1.10}$$

is the London penetration depth (where q is the charge, m is the particle mass, n_s is the particle density, and μ_0 is the permeability). In the following, we will deal with the penetration depth λ_L many times. With Eq. (1.10), we find

$$n\frac{h}{q} = \mu_0 \lambda_L^2 \oint \mathbf{j}_s \, \mathrm{d}\mathbf{r} + \Phi \tag{1.11}$$

Equation (1.11) represents the quantization of the fluxoid. The expression on the right-hand side denotes the "fluxoid." In many cases, the supercurrent density and, hence, the line integral on the right-hand side of Eq. (1.11) are negligibly small. This happens in particular if we deal with a thick-walled superconducting cylinder or with a ring made of a type-I superconductor. Because of the Meissner–Ochsenfeld effect, the magnetic field is expelled from the superconductor. The shielding supercurrents only flow near the surface of the superconductor and decay exponentially toward the interior, as we will discuss further below. We can place the integration path, along which Eq. (1.11) must be evaluated, deep in the interior of the ring. In this case, the integral over the current density is exponentially small, and we obtain in good approximation

$$\Phi \approx n\frac{h}{q} \tag{1.12}$$

However, this is exactly the condition for the quantization of the magnetic flux, and the experimental observation $\Phi = n(h/2|e|) = n\Phi_0$ clearly shows that the super-conducting charge carriers have the charge $|q| = 2e$. The sign of the charge carriers cannot be found from the observation of the flux quantization,

since the direction of the particle current is not determined in this experiment. In many superconductors, the Cooper pairs are formed by electrons, that is, $q = -2e$. On the other hand, in many high-temperature superconductors, we have hole conduction similar to that found in p-doped semiconductors. Here, we have $q = +2e$.

Next, we turn to a massive superconductor without any hole in its geometry. We assume that the superconductor is superconducting everywhere in its interior. Then we can imagine an integration path with an arbitrary radius placed around an arbitrary point, and again we obtain Eq. (1.11) similar to the case of the ring. However, now we can consider an integration path having a smaller and smaller radius *r*. It is reasonable to assume that on the integration path the supercurrent density cannot become infinitely large. However, then the line integral over $\mathbf{j}_s$ approaches zero, since the circumference of the ring vanishes. Similarly, the magnetic flux Φ, which integrates the magnetic field $\mathbf{B}$ over the area enclosed by the integration path, approaches zero, since this area becomes smaller and smaller. Here, we have assumed that the magnetic field cannot become infinite. As a result, the right-hand side of Eq. (1.11) vanishes, and we have to also conclude that the left-hand side must vanish, that is, $n = 0$, if we are dealing with a continuous superconductor.

Now we assume again a finite integration path, and with $n = 0$ we have the condition

$$\mu_0 \lambda_L^2 \oint \mathbf{j}_s \, d\mathbf{r} = -\Phi = -\int_F \mathbf{B} \, d\mathbf{f} \tag{1.13}$$

Using Stokes' theorem again, this condition can also be written as

$$\mathbf{B} = -\mu_0 \lambda_L^2 \operatorname{curl} \mathbf{j}_s \tag{1.14}$$

Equation 1.14 is the second London equation, which we will derive below in a slightly different way. It is one of two fundamental equations with which the two brothers F. London and H. London already in 1935 had constructed a successful theoretical model of superconductivity [24].

Next, we turn to the Maxwell equation $\operatorname{curl} \mathbf{H} = \mathbf{j}$, which we change to

$$\operatorname{curl} \mathbf{B} = \mu_0 \mathbf{j}_s \tag{1.15}$$

using $\mathbf{B} = \mu\mu_0\mathbf{H}$, $\mu \approx 1$ for non-magnetic superconductors and $\mathbf{j} = \mathbf{j}_s$. Again we take the curl of both sides of Eq. (1.15), replace $\operatorname{curl} \mathbf{j}_s$ with the help of Eq. (1.14), and continue to use the relation[10] $\operatorname{curl}(\operatorname{curl} \mathbf{B}) = \operatorname{grad}(\operatorname{div} \mathbf{B}) - \Delta\mathbf{B}$ and Maxwell's equation $\operatorname{div} \mathbf{B} = 0$. Thereby we obtain

$$\Delta\mathbf{B} = \frac{1}{\lambda_L^2}\mathbf{B} \tag{1.16}$$

This differential equation produces the Meissner–Ochsenfeld effect, as we can see from a simple example. For this purpose, we consider the surface of a very large

10) Notation: "div" is the divergence of a vector, $\operatorname{div} \mathbf{B} = \partial B_x/\partial x + \partial B_y/\partial y + \partial B_z/\partial z$; "grad" is the gradient, $\operatorname{grad} f(x, y, z) = (\partial f/\partial x, \partial f/\partial y, \partial f/\partial z)$; and Δ is the Laplace operator, $\Delta f = \partial^2 f/\partial x^2 + \partial^2 f/\partial y^2 + \partial^2 f/\partial z^2$. In Eq. (1.16) the latter must be applied to the three components of $\mathbf{B}$.

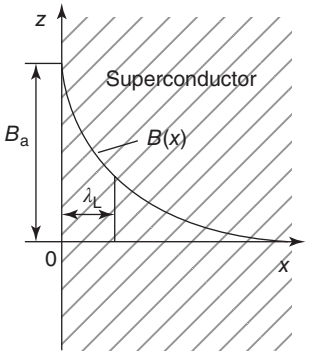

Figure 1.15 Decrease in the magnetic field within the superconductor near the planar surface.

superconductor, located at the coordinate $x = 0$ and extended infinitely along the (x, y) plane. The superconductor occupies the half-space $x > 0$ (see Figure 1.15). An external magnetic field $\mathbf{B}_a = (0, 0, B_a)$ is applied to the superconductor. Due to the symmetry of our problem, we can assume that within the superconductor only the z-component of the magnetic field is different from zero and is only a function of the x-coordinate. Equation 1.16 then yields for $B_z(x)$ within the superconductor, that is, for $x > 0$:

$$\frac{\mathrm{d}^2 B_z(x)}{\mathrm{d}x^2} = \frac{1}{\lambda_L^2} B_z(x) \tag{1.17}$$

This equation has the solution

$$B_z(x) = B_z(0) \times \exp(-x/\lambda_L) \tag{1.18}$$

which is shown in Figure 1.15. Within the length λ_L the magnetic field is reduced by the factor $1/e$, and the field vanishes deep within the superconductor.

We note that Eq. (1.17) also yields a solution increasing with x:

$$B_z(x) = B_z(0) \times \exp(+x/\lambda_L)$$

However, this solution leads to an arbitrarily large magnetic field in the superconductor and, hence, is not meaningful.

From Eq. (1.10) we can obtain a rough estimate of the London penetration depth with the simplifying assumption that one electron per atom with free-electron mass m_e contributes to the supercurrent. For tin, for example, such an estimate yields $\lambda_L = 26$ nm. This value deviates only little from the measured value, which at low temperatures falls in the range 25–36 nm.

Only a few nanometers away from its surface, the superconducting half-space is practically free of the magnetic field and displays the ideal diamagnetic state. The same can be found for samples with a more realistic geometry, for example, a superconducting rod, as long as the radii of curvature of the surfaces are much larger than λ_L and the superconductor is also much thicker than λ_L. Then on a length scale of λ_L, the superconductor closely resembles a superconducting half-space. Of course, for an exact solution, Eq. (1.16) must be solved.

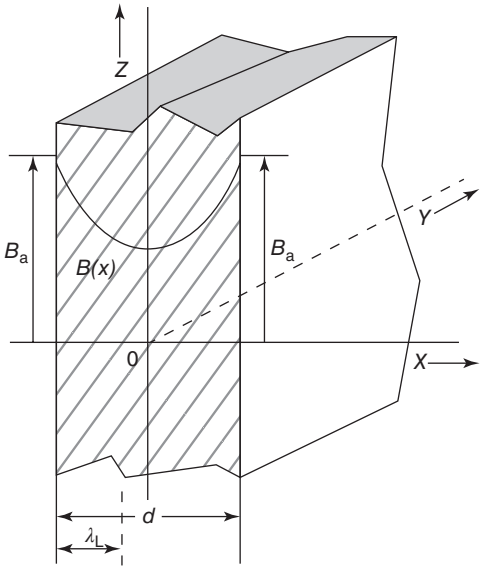

Figure 1.16 Spatial dependence of the magnetic field in a thin superconducting layer of thickness d. For the assumed ratio $d/\lambda_L = 3$, the magnetic field only decreases to about half of its outside value.

The London penetration depth depends on temperature. From Eq. (1.10) we see that λ_L is proportional to $1/n_s^{1/2}$. We can assume that the number of electrons combined into Cooper pairs decreases with increasing temperature and vanishes at T_c. Above the transition temperature, no stable Cooper pairs should exist anymore.[11] Hence, we expect that λ_L increases with increasing temperature and diverges at T_c. Correspondingly, the magnetic field penetrates further and further into the superconductor until it homogeneously fills the sample above the transition temperature.

We consider now in some detail a superconducting plate with thickness d. The plate is arranged parallel to the (y, z) plane, and a magnetic field B_a is applied parallel to the z-direction. This geometry is shown in Figure 1.16. Also in this case, we can calculate the spatial variation of the magnetic field within the superconductor using the differential equation (1.17). However, now the magnetic field is equal to the applied field B_a at both surfaces, that is, at $x = \pm d/2$. To find the solution, we have to also take into account the exponential function increasing with x. As an ansatz we chose the linear combination

$$B_z(x) = B_1 e^{-x/\lambda_L} + B_2 e^{+x/\lambda_L} \tag{1.19}$$

11) Here, we neglect thermal fluctuations by which Cooper pairs can be generated momentarily also above T_c. We will return to this point in Section 4.8.

For $x = d/2$, we find

$$B_a = B_z\left(\frac{d}{2}\right) = B_1 e^{-d/2/\lambda_L} + B_2 e^{+d/2\lambda_L} \tag{1.20}$$

Since our problem is symmetric for x and $-x$ for the chosen coordinate system, we have $B_1 = B_2 = B^*$ and we obtain

$$B_a = B^*(e^{d/2\lambda_L} + e^{-d/2\lambda_L}), \quad \text{with } B^* = \frac{B_a}{2\cosh(d/2\lambda_L)} \tag{1.21}$$

Hence, we find within the superconductor

$$B_z(x) = B_a \frac{\cosh(x/\lambda_L)}{\cosh(d/\lambda_L)} \tag{1.22}$$

This result is shown in Figure 1.16. For $d \gg \lambda_L$, the field decays exponentially in the superconductor away from the two surfaces, and the interior of the plate is nearly free of magnetic field. However, for decreasing thickness d the variation of the magnetic field becomes smaller and smaller, since the shielding layer cannot develop completely anymore. Finally, for $d \ll \lambda_L$, the field varies only little over the thickness. Now the field penetrates practically homogeneously through the superconducting layer.

For the cases of the superconducting half-space and of the superconducting plate, we also calculate the shielding current flowing within the superconductor. From the variation of the magnetic field, we find the density of the shielding current using the first Maxwell equation (1.15), which reduces to the equation $\mu_0 j_{s,y} = -(dB_z/dx)$ for $\mathbf{B} = (0, 0, B_z(x))$. Hence, the current density only has a y-component, which decreases from the surface toward the interior of the superconductor, similar to the magnetic field.

For the case of the superconducting half-space, one finds $j_{s,y} = (B_a/\mu_0\lambda_L)\, e^{-x/\lambda_L}$. Therefore, at the surface the current density is $B_a/\mu_0\lambda_L$. For the case of the thin plate we obtain $j_{s,y} = -(B_a/\mu_0\lambda_L)(\sinh(x/\lambda_L)/\cosh(d/\lambda_L))$, which reduces to $j_{s,y}(-d/2) = (B_a/\mu_0\lambda_L)\tanh(d/2\lambda_L)$ at the surface at $x = -d/2$. At $x = d/2$, the supercurrent density is the negative of this value.

We see that at $x = -d/2$ the supercurrents flow into the plane of the paper, and at $x = d/2$ they flow out of this plane. Noting that for a plate with finite size these currents must join together, we are dealing with a circulating current flowing near the surface around the plate. The magnetic field generated by this current is oriented in the direction opposite to that of the applied field. Hence, the plate behaves like a diamagnet.

How can one measure the London penetration depth? In principle, one must determine the influence of the thin shielding layer upon the diamagnetic behavior. This has been done using several different methods.

For example, one can determine the magnetization of thinner and thinner plates [25]. As long as the thickness of the plate is much larger than the penetration depth, one will find a nearly ideal diamagnetic result, which will decrease, however, if the plate thickness approaches the range of λ_L. Another method is μSR, which is sensitive to local magnetic fields, as discussed in Section 1.2. In order to

determine the penetration depth in the Meissner state, the muons are implanted into different depths by varying the implantation energy. In this way, one finds λ_L [26].

Other methods are based on the Shubnikov phase and determine λ_L from the diameter of the flux lines.

To determine the temperature dependence of λ_L, only relative measurements are needed. One can determine the resonance frequency of a cavity fabricated from a superconducting material. The resonance frequency depends sensitively on the geometry. If the penetration depth varies with the temperature, this is equivalent to a variation of the geometry of the cavity and, hence, of the resonance frequency, yielding the change of λ_L [27]. We will present experimental results in Section 4.5.

A strong interest in the exact measurement of the penetration depth, say, as a function of temperature, magnetic field, or the frequency of the microwaves for excitation, arises because of its dependence on the density of the superconducting charge carriers. It yields important information on the superconducting state and can serve as a sensor for studying superconductors.

Let us now return to our discussion of the macroscopic wave function. The concept of the coherent matter wave formed by the charge carriers in the superconducting state has already provided the explanation of ideal diamagnetism and of the fluxoid quantization or of flux quantization. Furthermore, we have found a fundamental length scale of superconductivity, namely the London penetration depth.

What causes the difference between type-I and type-II superconductivity and the generation of vortices? From the assumption of a continuous superconductor, we have obtained the second London equation and ideal diamagnetism. In type-I superconductors, this state is established as long as the applied magnetic field does not exceed a critical value. At higher fields superconductivity breaks down. For a discussion of the critical magnetic field, we must treat the energy of a superconductor more accurately. This will be done in Chapter 4. We will see that it is the competition between two energies, the energy gain from the condensation of Cooper pairs and the energy loss due to the magnetic field expulsion, which causes the transition between the superconducting and the normal conducting state.

At small magnetic fields, the Meissner phase is also established in type-II superconductors. However, at the lower critical field, vortices appear within the material. Turning again to Eq. (1.11), we see that the separation of the magnetic flux into units[12] of $\pm 1\Phi_0$ corresponds to states with quantum number $n = \pm 1$. However, the discussion of the Meissner state has also shown that the superconductor cannot display continuous superconductivity anymore. Instead, we must assume that the vortex axis is not superconducting, similar to the ring geometry. In this case, the integration path cannot be contracted to a point anymore, and the derivation of the second London equation with $n = 0$, resulting in the Meissner–Ochsenfeld effect, is no longer valid. A more

12) The sign must be chosen according to the direction of the magnetic field.

accurate treatment based on the Ginzburg–Landau theory shows that, on a length scale ξ_{GL}, the Ginzburg–Landau coherence length, superconductivity vanishes as one approaches the vortex axis (see also Section 4.7.2). Depending on the superconducting material, this length ranges between a few and a few hundred nanometers. Similar to the London penetration depth, it is temperature dependent, in particular close to T_c.

In the Shubnikov phase, the superconductor is penetrated by many normal conducting lines. However, why does each vortex carry exactly one flux quantum Φ_0? Again we must look at the energy of a superconductor. Essentially we find that in a type-II superconductor, it is energetically favorable if it generates a superconductor/normal conductor interface above the lower critical magnetic field (see Section 4.7). Therefore, as many of these interfaces as possible are generated. This is achieved by choosing the smallest quantum state with $n = \pm 1$, since in this case the maximum number of vortices and the largest interface area near the vortex axis is established.

We could use Eq. (1.11) for calculating how far the magnetic field of a flux line extends into the superconductor. However, we refrain from presenting this calculation. It turns out that also in this case the field decreases nearly exponentially with the distance from the vortex axis on the length scale λ_L. Hence, we can say that the flux line has a magnetic radius of λ_L.

Now we can also estimate the lower critical field B_{c1}. Each flux line carries a flux quantum Φ_0, and one needs at least a magnetic field $B_{c1} \approx \Phi_0/$(cross-sectional area of the flux line) $\approx \Phi_0/(\pi\lambda_L^2)$ to generate this amount of flux. With a value of $\lambda_L = 100\,\text{nm}$, one finds $B_{c1} \approx 66\,\text{mT}$.

For increasing magnetic field, the flux lines are packed closer and closer to each other, until near B_{c2} their distance is about equal to the Ginzburg–Landau coherence length ξ_{GL}. For a simple estimate of B_{c2}, we assume a cylindrical normal conducting vortex core. Then superconductivity is expected to vanish if the distance between the flux quanta becomes equal to the core diameter, that is, at $B_{c2} \approx \Phi_0/(\pi\xi_{GL}^2)$. An exact theory yields a value smaller by a factor of 2.[13] We note that, depending on the value of ξ_{GL}, B_{c2} can become very large. With the value $\xi_{GL} = 2\,\text{nm}$, one obtains a field larger than 80 T. Such high values of the upper critical magnetic field are reached or even exceeded in high-temperature superconductors.

At the end of this section, we wish to ask how permanent current and zero resistance, the key phenomena of superconductivity, can be explained in terms of the macroscopic wave function. Therefore, we look at the second London equation (1.14), $\mathbf{B} = -\mu_0\lambda_L^2 \operatorname{curl}\mathbf{j}_s$, and in addition we use Maxwell's equation

$$\operatorname{curl}\mathbf{E} = -\frac{d\mathbf{B}}{dt} = -\dot{\mathbf{B}} \tag{1.23}$$

connecting the curl of the electric field with the temporal change of the magnetic field. We take the time derivative of Eq. (1.14) and insert the result into Eq. (1.23).

13) Often one uses this relation for determining ξ_{GL}. Another possibility arises from the analysis of the conductivity near the transition temperature (see also Section 4.8).

Then we obtain $\operatorname{curl}\mathbf{E} = \mu_0\lambda_L^2 \operatorname{curl}\dot{\mathbf{j}}_s$ and, except for an integration constant,

$$\mathbf{E} = \mu_0\lambda_L^2 \dot{\mathbf{j}}_s \tag{1.24}$$

This is the first London equation. For a temporally constant supercurrent, the right-hand side of Eq. (1.24) is zero. Hence, we obtain current flow without an electric field and zero resistance.

Equation (1.24) also indicates that in the presence of an electric field the supercurrent density continues to increase with time. For a superconductor this seems reasonable, since the superconducting charge carriers are accelerated more and more due to the electric field. On the other hand, the supercurrent density cannot increase up to infinity. Therefore, additional energy arguments are needed to find the maximum supercurrent density that can be reached. In Section 5.1, we will present these arguments using the Ginzburg–Landau theory.

We could have derived the first London equation also from classical arguments, if we note that for current flow without resistance the superconducting charge carriers cannot experience (inelastic) collision processes. Then, in the presence of an electric field, we have the force equation $m\dot{\mathbf{v}} = q\mathbf{E}$. We use $\dot{\mathbf{j}} = qn_s\mathbf{v}$ and find $\mathbf{E} = (m/q^2n_s)\ \dot{\mathbf{j}}_s$. The latter equation can be turned into Eq. (1.24) using the definition (1.10) of the London penetration depth.

This argument indicates at least formally that the zero value of the resistance is also a consequence of the macroscopic wave function. However, we may also ask what processes lead to a finite resistance or cause the decay of a permanent current. For simplicity, we restrict our discussion to direct currents in a type-I superconductor, that is, we do not consider dissipative effects caused by vortex motion or by the acceleration of unpaired electrons in an alternating electric field.

We look at the strongly simplified situation shown in Figure 1.17. We assume the geometry of a metallic ring containing only four electrons. The electrons can move only along the ring. In this figure, the ring is shown after being cut and straightened into a piece of wire, the two ends of which are identical. Such a case is also referred to as a *periodic boundary condition.* An electron leaving the ring, say, on the left end, reappears again on the right end.

In the normal conducting state ($T > T_c$), the circulating current is assumed to be zero. However, this does not mean that the electrons are completely at rest. Because of the Pauli principle, the electrons must occupy different quantum states. If we neglect the electron spin, the four electrons must have different wave vectors and, hence, different velocities. We have marked these velocities by arrows with different lengths and different directions, which are attached to the electrons. As required by quantum mechanics, the wave numbers and, hence, the velocities of the electrons can change only in integer steps. This is indicated by the length of the arrows. If no net circulating current is assumed to flow, the velocities of the four electrons must cancel each other exactly. This is the situation shown in the upper left of the figure. On the other hand, if we have generated a circulating current, the electrons are moving predominantly in one direction. This is shown in the second

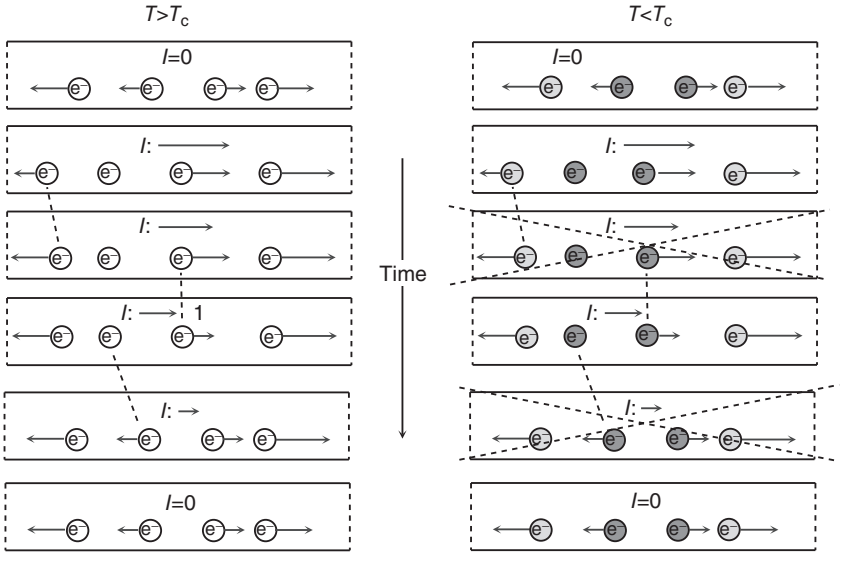

Figure 1.17 Generation of the supercurrent. Four electrons in a wire bent to a ring are shown.

picture from the top. Here, we have added one unit to the velocity of each electron, and the total current is indicated by the arrow of the sum.[14)]

If we leave the system alone, the electrons will change their quantum state very rapidly by means of collision processes toward the state with the smallest possible total energy. Hence, the circulating current will have decayed after a short time. In the figure a few collision processes are indicated, where we have marked the scattered electrons by a dashed line. Here, the total current can change in steps of one unit.

The macroscopic wave function is distinguished by the fact that the centers of mass of all Cooper pairs have the same momentum and the same wave vector. For illustration, on the right-hand side of Figure 1.17, the four electrons are combined into two Cooper pairs and are marked by dark or light gray color. We note that in the two upper pictures of the right-hand side, both pairs have the same velocity of the center of mass, respectively. For current $I = 0$, this velocity is zero. In the second picture the velocity vector of both pairs points to the right by one unit. Now a number of collision processes, resulting in the decay of the current at $T > T_c$, do not function anymore, since they violate the condition that the velocity of the centers of mass of both pairs must be the same. During a transition of one electron, the other electrons must adjust their quantum states in such a way that all pairs continue to have the same velocity of the centers of mass. The total current must change in steps of at least two units, until the state $I = 0$ is reached again. Similarly,

14) Here, we ignore the negative sign of the electron charge. Otherwise, we would have to reverse the direction of the current and velocity vectors.

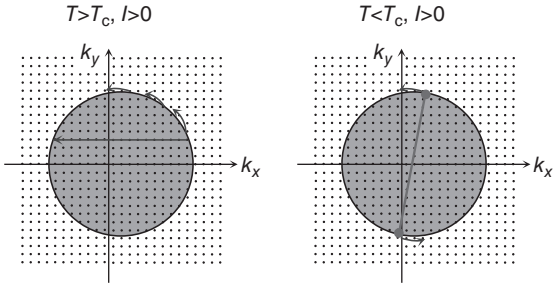

Figure 1.18 Generation of the supercurrent: current transport and decay of the permanent current illustrated with the Fermi sphere.

for N pairs, the total current must change in steps of N units. For $N = 2$ such events clearly would not be very unlikely. However, for 10^{20} electrons or Cooper pairs, the probability of such simultaneous processes would be extremely small, and the current does not decay.

We can illustrate the above arguments also more realistically with the Fermi sphere. In Figure 1.18 two dimensions k_x and k_y of $\mathbf{k}$-space are shown. The allowed discrete values of $\mathbf{k}$ are indicated by the individual dots (which are shown at a strongly exaggerated distance). At least for $T = 0$, the electrons occupy the states with the lowest energy, yielding the Fermi sphere for 3D and correspondingly a circle in the (k_x, k_y) plane. For zero net current flow, this sphere is centered around the origin of the coordinate system. If a net current is flowing in the x-direction, the Fermi sphere is slightly displaced parallel to k_x, since a net motion in the direction of the current must remain, if we sum over all electrons.[15] In Figure 1.18, this displacement is highly exaggerated.

In the normal conducting state with the observation of the Pauli principle, electrons can scatter into lower energy states essentially independently of each other (as indicated by the arrows), and the Fermi sphere rapidly relaxes back to the origin, that is, the circulating current decays quickly. However, in the superconducting state, the pairs are correlated with respect to the center of the Fermi sphere. They can only scatter around the sphere, without affecting the center of the sphere. Hence, the circulating current does not decay and we have a permanent current.

The simplest possibility for slowing down the circulating current in a ring containing many electrons arises by briefly eliminating the pair correlation in the smallest possible volume element of the ring by means of a fluctuation. This volume element would briefly be normal conducting, and the circulating current could decrease easily. We wish to estimate roughly the probability of such a process.

The length scale over which the superconductivity can be suppressed is the Ginzburg–Landau coherence length ξ_{GL}, which we have discussed already in conjunction with the vortices in type-II superconductors. The smallest volume that

15) Again we ignore the negative sign of the electron charge.

can briefly become normal is then given by the cross-section of the wire multiplied by ξ_{GL}, if the wire diameter does not exceed ξ_{GL}. We assume that the volume to become normal is $V_c = \xi_{GL}^3$. How many Cooper pairs are contained in this volume? The electron density is taken as n, and we assume that the fraction a of all electrons are paired. Then within the volume ξ_{GL}^3, there are $N_c = an\xi_{GL}^3/2$ pairs. According to the Bardeen–Cooper–Schrieffer (BCS) theory, the fraction a of electrons effectively participating in Cooper pairing is approximately given by Δ_0/E_F, where E_F is the Fermi energy and Δ_0 the energy gap. For metallic superconductors such as Nb or Pb, we have $\Delta_0 \approx 1$ meV and $E_F \approx 1$ eV. Hence, we find for the fraction $a \approx 10^{-3}$. If we take $n = 10^{23}$ cm^{-3} and $\xi_{GL} \approx 100$ nm, we obtain about 10^5 Cooper pairs to be transferred into the normal state by means of a fluctuation. The condensation energy per pair is also about 1 meV. Hence, the energy cost E_c of the above process is at least about 10^2 eV. From thermodynamics we know that the probability for this process is proportional to the Boltzmann factor $\exp(-E_c/k_B T)$. For a temperature of 1 K, we have $k_B T \approx 0.08$ meV, and for the ratio $E_c/k_B T$ we obtain about 10^6. Hence, the Boltzmann factor is only about $\exp(-10^6)$.

Here, we note that an exact analysis of the fluctuation effects leading to the appearance of a finite resistance in a thin superconducting wire is much more complicated than just described [28, 29]. However, the exponential dependence on the condensation energy within a coherence volume remains. This dependence has been tested by measurements of the resistance of very thin single-crystalline tin wires (so-called whiskers) near $T_c = 3.7$ K [30, 31]. Within 1 mK, the resistance dropped exponentially by 6 orders of magnitude. If we extrapolate this behavior to lower temperatures, we find the probability for a brief breakdown of superconductivity so extremely small that with good reason we can speak of the zero resistance.

For high-temperature superconductors, the condensation energy per pair is about 1 order of magnitude larger than for Nb or Pb. However, the volume V_c is much smaller. Here, the Ginzburg–Landau coherence length is anisotropic. In two spatial directions it is about 1–2 nm, and in the third direction it is smaller than 0.3 nm. Here, at low temperatures, the volume V_c may contain less than 10 Cooper pairs. In this case at $T = 1$ K, the Boltzmann factor is about $\exp(-10^2)$.

Indeed, in high-temperature superconductors, fluctuation effects often are not negligible and can lead to a number of interesting phenomena, in particular in conjunction with vortices. We will discuss this in more detail in Chapters 4 and 5.

1.5 Quantum Interference

How can we directly demonstrate the coherent matter wave in a superconductor? In optics this is elegantly done by means of diffraction experiments or interference. Everybody is familiar with the interference stripes produced, for example, by laser light passing through a double slit and then focused on a screen.

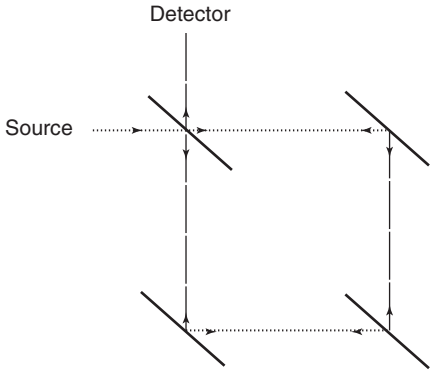

Figure 1.19 The optical Sagnac interferometer.

In Figure 1.19, a special optical interferometer, the Sagnac interferometer, is shown schematically. A laser beam is split in two by means of a semi-transparent mirror in such a way that the two partial waves travel along a "circular" path in opposite directions due to three additional mirrors. If two partial waves with the same phase reach the detector, the waves interfere constructively, and a large signal can be observed. It is the sensitivity with respect to a rotation of the measurement setup that makes the Sagnac interferometer so interesting. If the setup rotates, say, clockwise in the diagram, the mirrors move against the beam coming from the opposite direction. However, the mirrors move away from the beam coming along the same direction. Hence, the beam running clockwise must travel a larger distance before it hits the detector than the beam running counterclockwise. As a result, a phase difference between the partial waves appears at the detector. The detected signal is smaller. With faster and faster rotational velocity of the measurement setup, the signal is expected to vary periodically between a maximum and a minimum value. Because of this dependence of the detector signal upon the rotational velocity of the setup, one can use the Sagnac interferometer as a gyroscope for detecting rotational motion.

In principle, wave nature can be demonstrated also using *temporal* interference. Imagine that two waves having different frequencies interfere with each other, and that we observe the total amplitude of the two waves at a specific location, say, at $x = 0$. Each time when both waves are exactly in phase, the total amplitude of the wave is equal to the sum of the amplitudes of both partial waves. If both waves are exactly in the opposite phase, the total amplitude is equal to the difference of the amplitudes of the two partial waves. Hence, we observe that the amplitude of the total wave oscillates periodically with time, where the frequency is given by the difference of the oscillation frequencies of both partial waves.

Can similar phenomena occur in superconductors based on the coherent matter wave? The answer is yes: both phenomena, spatial and temporal interferences, can be observed and are utilized in many applications. For a more exact treatment, we must go a little further and first discuss the Josephson effect.

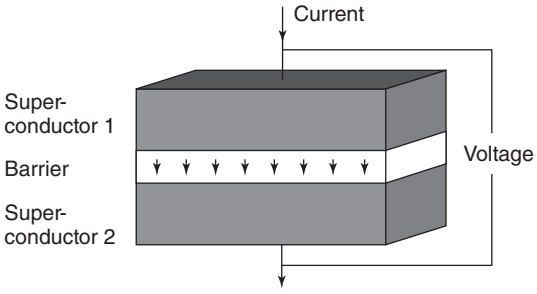

Figure 1.20 Sandwich geometry of two superconductors separated from each other by a thin barrier.

1.5.1
Josephson Currents

Imagine two superconductors placed on top of each other in the form of a sandwich structure. This arrangement is shown schematically in Figure 1.20. Between the two superconductors we imagine a non-superconducting barrier, for instance, an electrical insulator. If the barrier is sufficiently thin, about a few nanometers, electrons can pass from one superconductor to the other, although a non-conducting layer exists between the two metals. The reason is the quantum mechanical tunneling effect. The wave function, describing the probability of finding an electron, leaks out from the metallic region. If a second metal is brought into this zone, the electron can tunnel from metal 1 to metal 2, and a current can flow across this sandwich structure. This tunneling process is a highly fundamental phenomenon in quantum mechanics. For instance, it plays an important role in the alpha decay of atomic nuclei.

Due to the tunneling electrons or Cooper pairs, the two superconductors are coupled to each other, and a weak supercurrent, the Josephson current, can flow across the barrier. This current was theoretically predicted for the first time in 1962 by Josephson [32]. The Josephson current displays a number of surprising properties, which are closely connected with the phase of the macroscopic wave function in the superconducting state. In 1973, Josephson received the Nobel Prize for his discovery.

We will see that the Josephson current is proportional to the sine of the phase difference $\varphi_1 - \varphi_2$ of the macroscopic wave function of the two superconductors. More exactly, we have

$$I_c = I_c \sin \gamma \tag{1.25}$$

where γ is the gauge-invariant phase difference

$$\gamma = \varphi_2 - \varphi_1 - \frac{2\pi}{\Phi_0} \int_1^2 \mathrm{A}\,\mathrm{dl} \tag{1.26}$$

Here, the path integral of the vector potential is taken from superconductor 1 to superconductor 2 across the barrier.

Equation (1.25) is the first Josephson equation. The constant I_c is denoted as the critical current. Divided by the contact area, we have the critical current density j_c. At low temperatures, it typically falls in the range $10^2 - 10^4$ A/cm^2.

If a direct voltage U can be applied to the sandwich, as shown in Figure 1.20, the gauge-invariant phase difference increases as a function of time, as will be discussed in more detail below. In this case, we observe a high-frequency alternating current, the frequency of which is given by

$$f_J = \frac{U}{\Phi_0} = U\frac{2e}{h} \tag{1.27}$$

The alternating Josephson current represents the temporal interference of the wave functions of the two superconductors. The exact relation between the gauge-invariant phase difference γ and the applied voltage U is described by the second Josephson equation

$$\dot{\gamma} = \frac{2\pi}{\Phi_0}U \tag{1.28}$$

Below, the two Josephson equations will be derived in detail.

The frequency of the alternating Josephson current is proportional to the applied direct voltage, and the proportionality constant is the inverse of the flux quantum Φ_0. One finds a value of about 483.6 GHz/mV of applied voltage. This high value, and the fact that the oscillation frequency can be tuned using the applied voltage, makes Josephson junctions interesting as oscillators at frequencies in the high gigahertz range or even in the terahertz range. On the other hand, the fact that Eq. (1.27) connects voltage and frequency through the two fundamental constants h and e allows us to define voltage using the frequency of the alternating Josephson current and to utilize Josephson junctions as voltage standards. In Chapters 6 and 7, we will return to the many applications of Josephson junctions.

Now we look more exactly at the properties of the Josephson junction in terms of the macroscopic wave function. Similar to the case of individual electrons discussed earlier, we can imagine here also that the coherent matter wave is leaking out of the superconductor and in this way couples both superconducting parts.

Because of the great significance of the Josephson effect, we will derive the underlying "Josephson equations" in two different ways.

(1) The first derivation goes back to Feynman *et al.* [33]. One considers two weakly coupled quantum mechanical systems and solves the Schrödinger equation for this problem by means of an approximation. The magnetic field is neglected at this stage. The two *separate* systems will be described by the two wave functions Ψ_1 and Ψ_2. According to the time-dependent Schrödinger equation, for the temporal change of both wave functions, we have

$$\frac{\partial\Psi_1}{\partial t} = \frac{-i}{\hbar}E_1\Psi_1; \quad \frac{\partial\Psi_2}{\partial t} = \frac{-i}{\hbar}E_2\Psi_2 \tag{1.29}$$

If there is weak coupling between the systems, the temporal change of Ψ_1 will also be affected by Ψ_2 and vice versa. This situation can be taken into account by

introducing an additional coupling into Eq. (1.29):

$$\frac{\partial \Psi_1}{\partial t} = \frac{-i}{\hbar}(E_1 \Psi_1 + K\Psi_2) \tag{1.30a}$$

$$\frac{\partial \Psi_2}{\partial t} = \frac{-i}{\hbar}(E_2 \Psi_2 + K\Psi_1) \tag{1.30b}$$

In our case, the coupling means that Cooper pairs can be exchanged between the superconductors 1 and 2. The coupling strength is symmetric and is fixed by the constant K.

Compared to other quantum mechanical systems with two states (for instance, the H_2^+ molecule), a peculiarity of the two weakly coupled superconductors is the fact that Ψ_1 and Ψ_2 describe macroscopic states occupied by a large number of particles. Then we can interpret the square of the amplitude in terms of the particle density n_s of the Cooper pairs. Hence, we can write

$$\Psi_1 = \sqrt{n_{s1}}\, e^{i\varphi_1}; \quad \Psi_2 = \sqrt{n_{s2}}\, e^{i\varphi_2} \tag{1.31}$$

Here, φ_1 and φ_2 are the phases of the wave functions Ψ_1 and Ψ_2, respectively. Inserting these wave functions into Eqs. (1.30a) and (1.30b), we obtain

$$\frac{\dot{n}_{s1}}{2\sqrt{n_{s1}}}\, e^{i\varphi_1} + i\sqrt{n_{s1}}\, e^{i\varphi_1} \times \dot{\varphi}_1 = -\frac{i}{\hbar}\left\{E_1 \sqrt{n_{s1}}\, e^{i\varphi_1} + K\sqrt{n_{s2}}\, e^{i\varphi_2}\right\} \tag{1.32a}$$

$$\frac{\dot{n}_{s2}}{2\sqrt{n_{s2}}}\, e^{i\varphi_2} + i\sqrt{n_{s2}}\, e^{i\varphi_2} \times \dot{\varphi}_2 = -\frac{i}{\hbar}\left\{E_2 \sqrt{n_{s2}}\, e^{i\varphi_2} + K\sqrt{n_{s1}}\, e^{i\varphi_1}\right\} \tag{1.32b}$$

By separating the real and the imaginary parts, we find

$$\frac{1}{2}\frac{\dot{n}_{s1}}{\sqrt{n_{s1}}} = \frac{K}{\hbar}\sqrt{n_{s2}}\, \sin(\varphi_2 - \varphi_1) \tag{1.33a}$$

$$\frac{1}{2}\frac{\dot{n}_{s2}}{\sqrt{n_{s2}}} = \frac{K}{\hbar}\sqrt{n_{s1}}\, \sin(\varphi_1 - \varphi_2) \tag{1.33b}$$

$$i\sqrt{n_{s1}}\dot{\varphi}_1 = -\frac{i}{\hbar}\{E_1 \sqrt{n_{s1}} + K\sqrt{n_{s2}}\, \cos(\varphi_2 - \varphi_1)\} \tag{1.34a}$$

$$i\sqrt{n_{s2}}\dot{\varphi}_2 = -\frac{i}{\hbar}\{E_2 \sqrt{n_{s2}} + K\sqrt{n_{s1}}\, \cos(\varphi_1 - \varphi_2)\} \tag{1.34b}$$

If we also take into account that, because of the exchange of Cooper pairs between 1 and 2, we must always have $\dot{n}_{s1} = -\dot{n}_{s2}$, and if for simplicity we assume two identical superconductors (i.e., $n_{s1} = n_{s2}$), from Eqs. (1.33a) and (1.33b) we obtain the differential equation

$$\dot{n}_{s1} = \frac{2K}{\hbar} n_{s1}\, \sin(\varphi_2 - \varphi_1) = -\dot{n}_{s2} \tag{1.35}$$

The temporal change of the particle density in 1 multiplied with the volume V of 1 yields the change of the particle number and, hence, the particle current across

the junction. The electric current I_s is obtained by multiplication of the particle current with the charge $2e$ of each individual particle. Then we find

$$I_s = I_c \sin(\varphi_2 - \varphi_1) \tag{1.36}$$

with

$$I_c = \frac{2K \times 2e}{\hbar} V n_s = \frac{4\pi K}{\Phi_0} V n_s \tag{1.37}$$

This is the first Josephson equation, if we set the vector potential $\mathbf{A} = 0$. We recall that we had neglected magnetic fields. Therefore, this step is justified. Turning from n_s to the current within the junction, we must remember that both superconductors are connected to a current source, which serves to keep n_s constant within the superconductors by supplying or accepting the charges.

From Eqs. (1.34a) and (1.34b) one obtains a differential equation for the temporal change of the phase difference. With $n_{s1} = n_{s2}$ and $E_2 - E_1 = 2eU$, we have

$$\frac{\mathrm{d}}{\mathrm{d}t}(\varphi_2 - \varphi_1) = \frac{2eU}{\hbar} = \frac{2\pi}{\Phi_0} U \tag{1.38}$$

This is the second Josephson equation for the case $\mathbf{A} = 0$. We see that, for a temporally constant voltage $U =$ constant, the phase difference increases linearly with time:

$$\varphi_2 - \varphi_1 = \frac{2\pi}{\Phi_0} Ut + \varphi(t = 0) \tag{1.39}$$

However, this means that according to the first Josephson equation an alternating current appears in the junction, the frequency f of which is given by Eq. (1.27).

(2) The second derivation of the Josephson equations that we want to discuss in part goes back to Landau and Lifschitz [34]. It is based only on very general symmetry and invariance principles and thereby emphasizes the wide range of validity of the Josephson effect.

We start by considering qualitatively how supercurrent density and phase are connected to each other within a homogeneous superconducting wire.[16] The current is assumed to flow in the z-direction. It is convenient to write the supercurrent density as $j_{s,z} = 2en_s v_z$. We have used this relation already for the derivation of the fluxoid quantization. If we eliminate v_z by using the canonical momentum, Eq. (1.5), we obtain

$$j_{s,z} = \frac{q}{m} n_s (p_{\mathrm{can},z} - qA_z)$$

or by using $\mathbf{p}_{\mathrm{can}} = \hbar\mathbf{k}$

$$j_{s,z} = \frac{q}{m} n_s (\hbar k_z - qA_z)$$

16) These qualitative arguments treat the quantum mechanics only in a rough way, but yield the correct result.

We consider a matter wave of the form $\Psi = \Psi_0\, e^{i\varphi} = \Psi_0\, e^{i\mathbf{k}\cdot\mathbf{x}}$ and, instead of k_z, we write the expression $\varphi' \equiv d\varphi/dz$ (the derivative of the phase $\varphi = \mathbf{k}\cdot\mathbf{x}$ with respect to z yields k_z). Then we obtain

$$j_{s,z} = \frac{q}{m} n_s(\hbar\varphi' - qA_z) \tag{1.40}$$

Now we define

$$\gamma(z) = \varphi(z) - \frac{q}{\hbar}\int_0^z A_z\, dz \tag{1.41}$$

yielding

$$j_{s,z} = \frac{q\hbar}{m} n_s \times \gamma' \tag{1.42}$$

What happens if our superconducting wire has a weakened location, where the Cooper pair density is strongly reduced? This geometry is shown schematically in Figure 1.21. The current passing through the wire must have the same value everywhere. If we assume a constant supercurrent density over the cross-section of the wire, in Eq. (1.42) the product $n_s\gamma'$ must have the same value everywhere. However, if n_s is strongly reduced at the weakened location, there γ' must be much larger than in the remainder of the wire. If at the weakened location γ' displays a sharp peak, $\gamma(z)$ changes there very rapidly from a value γ_1 to a much larger value γ_2.

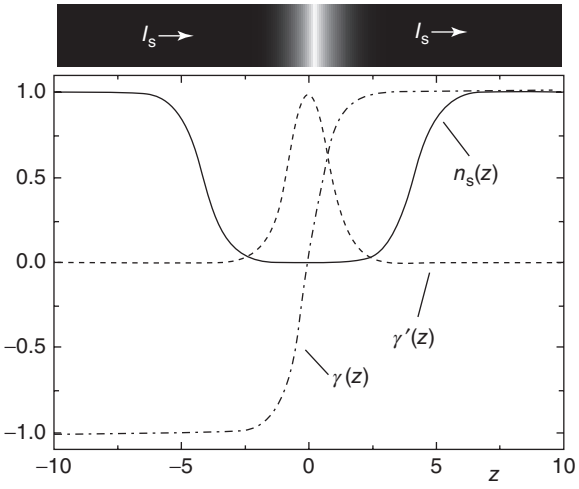

Figure 1.21 Derivation of the Josephson equations. We consider a thin superconducting wire with a weakened location at $z = 0$, at which the Cooper pair density n_s is strongly reduced. Due to current conservation, we have $n_s(z)\gamma'(z) = \text{constant}$, leading to a peak in $\gamma'(z)$ and to a step in γ. For illustration we have used the following "test function": $n_s(z) = 1/\gamma'(z) = 1/[1.001 - \tanh^2(x)]$, constant = 0.001. For $\gamma(z)$ one finds $\gamma(z) = \tanh(z) + 0.001z$. At the weakened location, $\gamma(z)$ changes very rapidly from −1 to +1.

Using Eq. (1.41), we can write the jump of the phase at the barrier as

$$\gamma = \gamma(z_2) - \gamma(z_1) = \varphi(z_2) - \varphi(z_1) - \frac{q}{\hbar}\int_{z_1}^{z_2} A_z \, \mathrm{d}z \tag{1.43}$$

where z_1 denotes a coordinate in superconductor 1 in front of the barrier and z_2 a coordinate in superconductor 2 behind the barrier. Equation (1.43) has exactly the same form as Eq. (1.26).

If we specify the spatial dependence $n_s(z)$, the supercurrent across the barrier is a function of the jump γ of the phase, that is, $I_s = I_s(\gamma)$. However, a change of the phase difference of 2π should yield the same wave function and, hence, the same value of the supercurrent across the barrier. Therefore, we can expand I_s as a sum of sine and cosine terms (a Fourier series):

$$I_s(\gamma) = \sum_{n=0}^{\infty} I_{cn} \sin(n\gamma) + \sum_{n=0}^{\infty} \widetilde{I}_{cn} \cos(n\gamma) \tag{1.44}$$

Here, I_{cn} and $\widetilde{I}_{cn}$ are the expansion coefficients of the function $I_s(\gamma)$. We note that microscopic details such as the structure of the barrier or the temperature dependence of the Cooper pair density are contained in these expansion coefficients. However, the periodicity of $I_s(\gamma)$ is independent of this.

Now we utilize the principle of time inversion symmetry. Many fundamental phenomena in Nature are reversible. If we record such a phenomenon with a camera and then run the motion picture backward, we see again a process that is physically possible.[17] Now we assume that this principle also applies to the Josephson current. If the time is reversed, the current flows backward, that is, we have a current $-I_s$. The macroscopic wave functions oscillate according to $\exp(-i\omega t)$. If the time is reversed here also, we see that also the sign of the phase of the wave function must be reversed. So if we request that the Josephson current be invariant under time reversal, we have the condition $I_s(\gamma) = -I_s(-\gamma)$. This eliminates all the cosine terms in Eq. (1.44).

Under time inversion symmetry, the supercurrent across the barrier is described by

$$I_s(\gamma) = \sum_{n=0}^{\infty} I_{cn} \sin(n\gamma) \tag{1.45}$$

Very often, but not necessarily, one finds that this series converges very rapidly, that is, the expansion coefficients become smaller very quickly. Then the series can be restricted to the first term, and we obtain the first Josephson equation.

At this stage, we note that there are situations for which the first expansion coefficient I_{c1} vanishes, for example. In this case, the relation between the supercurrent and the phase difference γ has period π instead of 2π.

17) This is not valid for irreversible processes. A full glass of water falling to the ground breaks into many pieces, and the water spreads over the floor. The inverse process, where the water and the broken pieces jump upon the table and reassemble to an unbroken glass filled with water, only exists in the motion picture.

To obtain the second Josephson equation, we take the time derivative of Eq. (1.43), and we obtain

$$\dot{\gamma} = \dot{\varphi}(z_2) - \dot{\varphi}(z_1) - \frac{q}{\hbar}\int_{z_1}^{z_2} \dot{A}_z \, \mathrm{d}z \tag{1.46}$$

According to the laws of electrodynamics, the integral over the time derivative of the vector potential yields exactly the voltage induced across the barrier by a temporally changing magnetic field. The time derivative of the difference $\varphi(z_2) - \varphi(z_1)$, with $\Psi \propto \exp(-i\omega t) = \exp(-iEt/\hbar)$, yields the difference $[E(z_2) - E(z_1)]/\hbar$ between the two superconductors on both sides of the barrier. We can write this difference as $q\ U_{21}$, with the voltage difference U_{21}. So we have

$$\dot{\gamma} = \frac{q}{\hbar}(U_{21} + U_{\mathrm{ind}}) = \frac{q}{\hbar}U_{\mathrm{total}} \tag{1.47}$$

With $q = 2e$, this yields the second Josephson equation (1.28).

The second derivation of the Josephson equations is very general. It was assumed that there exists a macroscopic wave function with a well-defined phase φ, and that the system satisfies time inversion symmetry. Equations 1.40 – 1.47 are also gauge-invariant.

The gauge invariance represents a highly fundamental principle. In the force and field equations of electrodynamics, only the electric and magnetic fields appear, not the corresponding potentials, the vector potential $\mathbf{A}$ and the scalar potential Φ. From the latter, one obtains the (negative) electric field by forming the gradient. We have mentioned already that curl $\mathbf{A} = \mathbf{B}$. However, the magnetic field is source-free, that is, we have div $\mathbf{B} = 0$. Therefore, a vector $\mathbf{V}(x,y,z,t)$, obtained from the gradient of a function $\chi(x, y, z, t)$, can be added to $\mathbf{A}$. This corresponds to a different scaling of $\mathbf{A}$. The curl of $\mathbf{V}$ always vanishes, and, hence, the magnetic field remains unaffected. However, in order also to keep the electric field unchanged during this transformation, at the same time we must subtract the quantity $\chi(x,y,z,t)$ from the scalar potential. Finally, in the Schrödinger equation, the phase φ of the wave function must be rescaled to $\varphi + (2\pi/\Phi_0)\chi$. The gauge invariance of Eqs. (1.40 – 1.47) can be shown by explicitly inserting these relations.

Often, equations showing gauge invariance are of fundamental importance in physics and cannot be affected easily by microscopic details. Hence, we can expect that the Josephson equations are generally valid in the case of many different types of barriers and superconductors.

In Figure 1.22, some types of junctions are shown schematically. For the superconductor – insulator – superconductor (SIS) junction (Figure 1.22a), the insulating barrier must be only 1 – 2 nm thick. The superconductor – normal conductor – superconductor (SNS) junction (Figure 1.22b) can function with a much larger thickness of the normal conductor, simply because the Cooper pairs can penetrate much deeper into a normal conducting metal than into an oxide layer. Here, in the normal metal, the decay length of the Cooper pair concentration depends among other things on the electron mean free path. For very large values of the electron mean free path (small amount of perturbations),

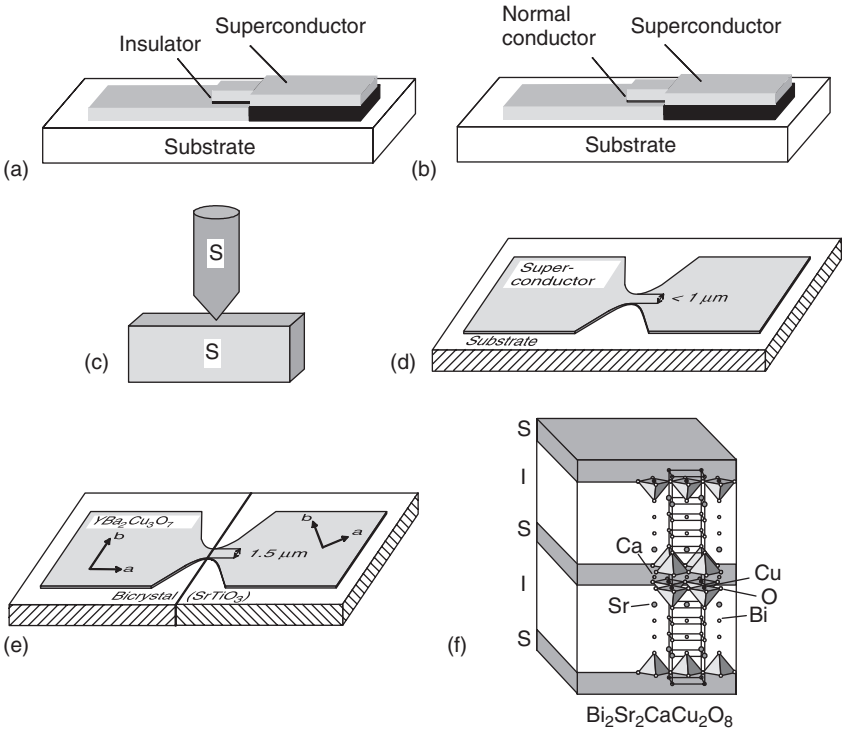

Figure 1.22 Schematics of the different possibilities for producing a weak coupling between two superconductors: (a) SIS junction with an oxide layer as a barrier; (b) SNS junction with a normal conducting barrier; (c) point contact; (d) microbridge; (e) $YBa_2Cu_3O_7$ grain boundary junction; and (f) intrinsic Josephson junction in $Bi_2Sr_2CaCu_2O_8$.

normal conducting layers with a thickness up to a few hundred nanometers can be used. An important difference between the oxide and the normal conductor junctions is the value of the resistance per square (normal resistance/area of the barrier). For the oxide junctions, the value of the resistance per square is typically $10^{-4}-10^{-3}\,\Omega\,\mathrm{cm}^2$. However, for the SNS junctions, this value is about $10^{-8}\,\Omega\,\mathrm{cm}^2$ or below. In addition to the SIS and SNS junctions, one often also uses junctions with a more complicated structure of the barrier, for instance, the so-called SINIS junctions where the barrier is formed by two insulators and one normal conducting layer.

The point contacts (Figure 1.22c) are particularly simple. In this case, a metal tip is pressed against a surface. The cross-section of the bridge depends on the applied pressure. In this way, the desired junction properties can be produced easily and can be adjusted if necessary. The microbridge (Figure 1.22d) only consists of a narrow constriction that limits the exchange of Cooper pairs because of its very small cross-section. Here, it is necessary to fabricate reproducibly bridges with

a width of only 1 μm or smaller, which requires advanced structuring techniques such as electron beam lithography.

For the high-temperature superconductors, one can use grain boundaries as weak coupling regions because of the small values of the coherence length [35, 36]. One can deposit a thin film, say, of $YBa_2Cu_3O_7$ on a "bicrystal substrate," consisting of two single-crystalline parts joined together at a specific angle. The grain boundary of the substrate is then transferred also into the deposited film, which otherwise is grown single-crystalline (epitaxially, Figure 1.22e). Well-defined grain boundaries can also be produced at steps in the substrate or at the edges of buffer layers epitaxially deposited on a substrate. The strength of the Josephson coupling can be varied over a large range by means of the grain boundary angle.

In some high-temperature superconductors such as, for instance, $Bi_2Sr_2CaCu_2O_8$, even intrinsic Josephson junctions exist simply because of their crystal structure (Figure 1.22f). Here, the superconductivity is restricted only to the copper oxide layers with about 0.3 nm thickness. Between these layers, there are electrically insulating bismuth oxide and strontium oxide planes. Hence, such materials form stacks of SIS Josephson junctions, where each junction has a thickness of only 1.5 nm, the distance between two neighboring copper oxide layers [37].

These highly different types of Josephson junctions only represent a small selection of the many possibilities. Each type of junction has its advantages and disadvantages. Depending on the specific application, quite different types can be utilized.

At this stage, we are confronted with the following question: How similar are the Josephson effects in these junctions, in particular, with respect to the connection between the oscillation frequency of the alternating Josephson currents and the applied voltage? The proportionality factor $1/\Phi_0$, which is also referred to[18] as the "*Josephson constant*" $K_J = 2e/h = 483.5979\,\text{GHz/mV}$, has been determined for many different types of Josephson junctions. For example, a Josephson junction made of indium with its weak location realized by a constriction (microbridge) has been compared directly with a Josephson junction made of niobium where the barrier consisted of a thin gold layer [38]. The Josephson constants measured for both junctions were equal within an uncertainty of only 2×10^{-16} or less. In the meantime, this accuracy could be increased even to about 10^{-19}. Therefore, Josephson junctions are now applied for representing the voltage standard [39].

How can we demonstrate alternating Josephson currents experimentally? A very direct method is the observation of the electromagnetic radiation generated by the oscillating Josephson currents in the frequency range of microwaves. We want to estimate the order of magnitude of the microwave power emitted from the junction.

We assume a voltage of 100 μV applied to the junction, corresponding to an emitted frequency of about 48 GHz. The critical current I_c of the junction is

18) The value given here was defined internationally in 1990 as the Josephson constant $K_{J\text{-}90}$, and therefore is exact.

assumed to be 100 μA. Then the d.c. power applied to the junction is 10^{-8} W, and the emitted power is expected to be much smaller than this value.

The difficulty of direct experimental demonstration did not so much arise because of the small power of this radiation, but, instead, it had to do with the problem of coupling the high-frequency power from the tiny tunnel junction into a proper high-frequency waveguide. Therefore, the first confirmation of the alternating Josephson current came in an indirect way [40]. If such a junction is placed within the high-frequency field of an oscillating microwave cavity, characteristic, equidistant steps of constant voltage are observed in the voltage–current characteristic (see Section 6.3). On the voltage axis, their distance ΔU is given by

$$\Delta U_S = \Phi_0 \times f_{HF} \tag{1.48}$$

where f_{HF} is the frequency of the high-frequency field. These "Shapiro steps" result from the superposition of the alternating Josephson current and the microwave field. Each time that the frequency of the alternating Josephson current corresponds to an integer multiple of the microwave frequency, the superposition produces an additional d.c. Josephson current, causing the step structure of the characteristic.

Another indirect confirmation of the existence of an alternating Josephson current was found for junctions placed within a small static magnetic field. Here, at small voltages U_s, equidistant steps in the characteristic could be observed without irradiation by an external high-frequency field (see Section 6.4). The sandwich geometry of a Josephson tunnel junction by itself represents a resonating cavity, and the structures observed in the characteristic, the "Fiske steps," correspond to resonances within the junction. For the proper values of the voltage U_s and of the field B, the Josephson oscillations of the current density exactly fit a cavity mode of the junction. For such a resonance, the current becomes particularly large.

A more accurate description of the Shapiro and Fiske modes requires a mathematical treatment beyond the scope of this first chapter. However, in Chapter 6, we will return to these structures.

In 1965 Ivar Giaever[19] achieved a more direct confirmation of the alternating Josephson current [41]. As we have seen, the main difficulty with the direct confirmation, say, with a typical high-frequency apparatus, arose from the extraction of power out of the small tunnel junction. Giaever had the idea that a second tunnel junction, placed immediately on top of the Josephson junction, would be quite favorable for such an extraction (Figure 1.23).

Here, the confirmation of the extracted power happens in the second tunnel junction by means of the change of the characteristic of the tunneling current for individual electrons, this change being caused by the irradiating high-frequency field generated in the Josephson junction. In the years prior to this, it had been shown that a high-frequency field generates a structure in the characteristic of the

19) For his experiments with superconducting tunnel junctions, Giaever received the Nobel Prize in 1973, together with B. D. Josephson and L. Esaki.

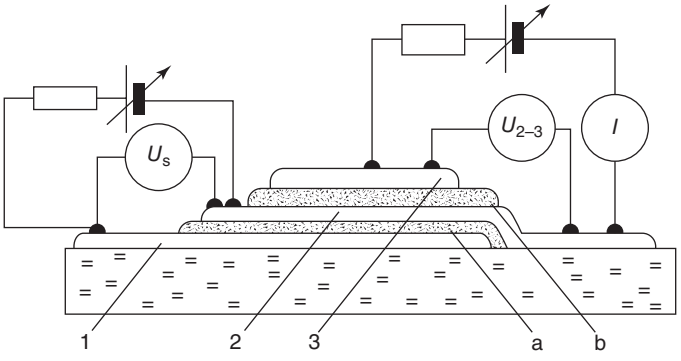

Figure 1.23 Arrangement for the experimental demonstration of the alternating Josephson current according to Giaever: layers 1–3 are Sn layers; layers a and b are oxide layers. The thicknesses of layers a and b are chosen such that layers 1 and 2 form a Josephson junction, and such that no Josephson currents are possible between layers 2 and 3. (From [40].)

single-electron-tunneling current [42]. The electrons can interact with the high-frequency field by absorbing or emitting photons with energy $E = hf_{\mathrm{HF}}$.

In Section 3.1.3 we will see that, in the absence of a high-frequency field, individual electrons can tunnel in large numbers between the two superconductors only after the voltage $(\Delta_1 + \Delta_2)/e$ has been reached. Here, Δ_1 and Δ_2 denote the energy gaps of the two superconductors, respectively, the magnitudes of which depend on the material. In other words, during the tunneling process, the electrons must take up at least the energy $eU = (\Delta_1 + \Delta_2)$. Then at the voltage $(\Delta_1 + \Delta_2)/e$, the voltage–current characteristic displays a sharp step as seen in Figure 1.23.

In a high-frequency field, a tunneling process assisted by photons can set in already at the voltage $U_s = (\Delta_1 + \Delta_2 - hf_{\mathrm{HF}})/e$. If during a tunneling process an electron absorbs several photons, one obtains a structure in the characteristic with the specific interval of the voltage U_s

$$\Delta U_s = \frac{hf_{\mathrm{HF}}}{e} \tag{1.49}$$

where h is the Planck's constant, f_{HF} is the frequency of the high-frequency field, and e is the elementary charge. Such processes can happen at high photon densities, that is, at high power of the high-frequency field. We note that for single-electron tunneling, the elementary charge e of single electrons appears.

At the junction 2–3, one observes a typical single-electron characteristic if no voltage is applied to the junction 1–2 (curve 1 in Figure 1.24). For performing the key experiment, a small voltage U_s is applied to the Josephson junction 1–2. If the expected high-frequency alternating current appears in this junction, in the junction 2–3 the well-known structure of the tunneling characteristic should be observed, because of the close coupling between the two junctions. Giaever, indeed, could observe this expected effect. Such a characteristic is shown by curve 2 in Figure 1.24. Here a voltage U_s of 0.055 mV was applied to junction 1–2,

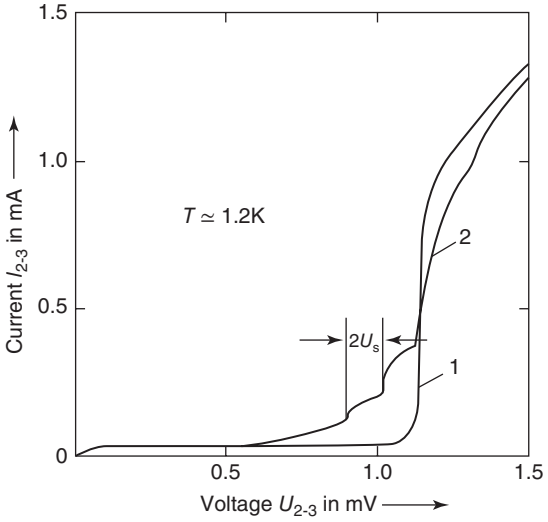

Figure 1.24 Characteristic of the junction 2–3 from Figure 1.22. Curve 1: no voltage at junction 1–2. Curve 2: 0.055 mV applied to junction 1–2.

acting as the generator of the high-frequency field. The frequency of the alternating Josephson current is $f_J = 2eU_s/h$, and the structure of the characteristic of junction 2–3 should display the voltage steps with the distance between them $\Delta U_s = hf_J/e = 2U_s$. For the curve shown in Figure 1.24, this yields $\Delta U_{2,3} = 0.11$ mV, which was observed by Giaever.

The most direct detection of the alternating Josephson current by coupling the power into a high-frequency waveguide has been achieved by an American and a Russian group. The Americans [43] could detect the high-frequency power of the Josephson junction by placing the junction into a tuned resonating cavity, which was operated at a resonance frequency of the junction by choosing a proper value of the magnetic field. However, this still required an extremely high detection sensitivity. The detected power was about 10^{-11} W, whereas the sensitivity limit for detection could be increased up to 10^{-16} W. The Russian group, Yanson *et al.* [44], could detect a radiation power of about 10^{-13} W of a Josephson junction. The relation $f_J = 2eU_s/h$ has always been found between the frequency of the alternating Josephson current and the voltage applied to the junction. The experimental accuracy has been increased by the American group sufficiently far that a precision measurement of $2e/h$ could be carried out [45]. This represented further convincing proof of the importance of electron pairs in superconductivity.

Today, the techniques for the detection of electromagnetic radiation are improved to such an extent that the alternating Josephson current can be extracted without any difficulty up to the 100 GHz range. However, there are still problems at frequencies in the terahertz range, which play an important role, for instance, in the intrinsic Josephson junctions of high-temperature superconductors. In the meantime, also this emission was detected. [54, 55]

In the future, Josephson junctions are expected to play an important role in the terahertz range. On the one hand, this frequency range is too high to be covered by semiconductor devices, and on the other, it is too low to be handled by optical methods.

1.5.2 Quantum Interference in a Magnetic Field

In the alternating Josephson currents, the macroscopic wave function manifests itself in the form of a *temporal* interference between the matter waves in the two superconducting electrodes. What can we say about the *spatial* interference, say, analogous to the optical double-slit experiment or to the Sagnac interferometer?

Let us look at the structure shown in Figure 1.25. It consists of a superconducting ring into which two Josephson junctions are integrated. The ring is located in a magnetic field oriented perpendicular to the area of the ring. A transport current I flows along the ring. By measuring the voltage drop across the Josephson junctions, we can determine the maximum supercurrent that can be carried by the ring. We will see that this maximum supercurrent $I_{s,max}$ oscillates as a function of the magnetic flux through the ring, similar to the light intensity, or more exactly the light amplitude, on the screen of the double-slit experiment, and also similar to the Sagnac interferometer with its dependence on the rotational frequency.

In Section 1.3, we looked at a superconducting ring placed in a magnetic field and we found that the magnetic flux through the ring appears in multiples of the flux quantum Φ_0. An arbitrary magnetic field $\mathbf{B}_a$ could be applied to the ring, generating an arbitrary magnetic flux Φ_a through the ring. However, in this case, a circulating current J flows along the ring. It also generates a magnetic flux $\Phi_{ind} = LJ$,

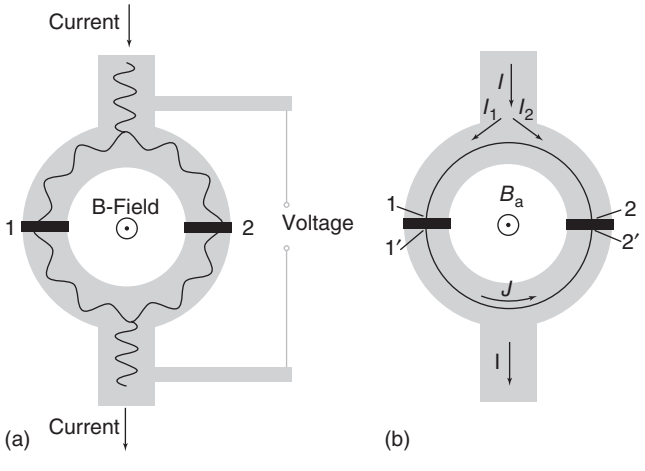

Figure 1.25 Generation of spatial interferences of the superconducting wave function in a ring structure. (a) Schematics of the wave. (b) Notation for the derivation of the quantum interference.

such that the total flux amounts to a multiple of Φ_0: $\Phi_{tot} = \Phi_a + LJ$. The circulating current results in a shift of Φ_a upward or downward to the next integer value of Φ_{tot}/Φ_0. Apparently, LJ must then reach a maximum value up to $\Phi_0/2$.

This picture is changed because of the insertion of the two Josephson junctions. At both Josephson junctions, the phase of the superconducting wave function can jump by amounts γ_1 or γ_2, which must be taken into account in the integration of the phase gradient around the ring (integral $\oint \mathbf{k}\,\mathrm{d}\mathbf{x}$). The jumps of the phase are connected with the current across the junctions because of the first Josephson equation (1.25).

Next, we derive the dependence $I_{s,max}(\Phi_a)$ using the notation of Figure 1.25b. We assume that the width of the Josephson junctions is much smaller than the diameter of the ring. The current I separates into the currents I_1 and I_2, flowing along the two halves of the ring, respectively. Because of current conservation, we have

$$I = I_1 + I_2 \tag{1.50}$$

The currents I_1 and I_2 can also be written in terms of the circulating current J flowing in the ring yielding

$$I_1 = \frac{I}{2} + J; \quad I_2 = \frac{I}{2} - J \tag{1.51}$$

The current I_1 flows through the Josephson junction 1, and the current I_2 through the Josephson junction 2. Therefore, we have

$$I_1 = I_c \sin\gamma_1; \quad I_2 = I_c \sin\gamma_2 \tag{1.52}$$

Here, for simplicity, we have assumed that the critical currents I_c of the two Josephson junctions are identical. Therefore, we find

$$\frac{I}{2} + J = I_c \sin\gamma_1 \tag{1.53a}$$

$$\frac{I}{2} - J = I_c \sin\gamma_2 \tag{1.53b}$$

Next, we need a relation connecting the gauge-invariant phase differences γ_1 and γ_2 with the applied magnetic field. We proceed analogously to the derivation of the quantization of the fluxoid (Eq. (1.11)), but we do not integrate the wave vector $\mathbf{k}$ over the complete ring, as in Eq. (1.7). Instead, we integrate separately over the lower and upper halves, that is, from 1′ to 2′ or from 2 to 1 in Figure 1.25b. Then we obtain

$$\int_{1'}^{2'} \mathbf{k}\,\mathrm{d}\mathbf{r} = \mu_0\lambda_L^2 \int_{1'}^{2'} \mathbf{j}_s\,\mathrm{d}\mathbf{r} + \frac{2\pi}{\Phi_0}\int_{1'}^{2'} \mathbf{A}\,\mathrm{d}\mathbf{r} \tag{1.54a}$$

$$\int_{2}^{1} \mathbf{k}\,\mathrm{d}\mathbf{r} = \mu_0\lambda_L^2 \int_{2}^{1} \mathbf{j}_s\,\mathrm{d}\mathbf{r} + \frac{2\pi}{\Phi_0}\int_{2}^{1} \mathbf{A}\,\mathrm{d}\mathbf{r} \tag{1.54b}$$

Here, we have used the definition 1.10 of the London penetration depth and $\Phi_0 = h/q = h/2e$.

The integral $\int_{1'}^{2'} \mathbf{k}\,\mathrm{d}\mathbf{r}$ yields the difference between the phase φ_2 of the wave function of the lower half of the ring, $\Psi_2 \sim \exp(ik{\cdot}r) = \exp(i\varphi_2)$ at the locations $2'$ and $1'$, $\int_{1'}^{2'} \mathbf{k}\,\mathrm{d}\mathbf{r} = \varphi_2(2') - \varphi_2(1')$. Analogously, one finds $\int_2^1 \mathbf{k}\,\mathrm{d}\mathbf{r} = \varphi_1(1) - \varphi_1(2)$. By adding Eqs. (1.54a) and (1.54b), we obtain

$$\varphi_2(2') - \varphi_1(2) - [\varphi_2(1') - \varphi_1(1)] = \mu_0 \lambda_\mathrm{L}^2 \left(\int_{1'}^{2'} \mathbf{j}_\mathrm{s}\,\mathrm{d}\mathbf{r} + \int_2^1 \mathbf{j}_\mathrm{s}\,\mathrm{d}\mathbf{r} \right) + \frac{2\pi}{\Phi_0} \oint_{C'} \mathbf{A}\,\mathrm{d}\mathbf{r} \tag{1.55}$$

Here, the integral over the curve C' does not include the barriers of the two Josephson junctions. Otherwise, the integral would run over the complete ring, and by using Stokes' theorem we could turn it into the magnetic flux through the ring. However, we can accomplish this by adding the integrals over the corresponding distances on both sides of Eq. (1.55). Then we find

$$\oint_{C'} \mathbf{A}\,\mathrm{d}\mathbf{r} + \int_{2'}^{2} \mathbf{A}\,\mathrm{d}\mathbf{r} + \int_{1}^{1'} \mathbf{A}_r\,\mathrm{d}\mathbf{r} = \oint_{C} \mathbf{A}\,\mathrm{d}\mathbf{r} = \int_F \mathbf{B}\,\mathrm{d}\mathbf{f} = \Phi \tag{1.56}$$

On the left-hand side of Eq. (1.55), the term

$$\varphi_2(2') - \varphi_1(2) + \frac{2\pi}{\Phi_0} \int_{2'}^{2} \mathbf{A}\,\mathrm{d}\mathbf{r}$$

yields the gauge-invariant phase difference γ_2 across the Josephson junction 2. Analogously, the expression

$$\varphi_2(1') - \varphi_1(1) - \frac{2\pi}{\Phi_0} \int_{1}^{1'} \mathbf{A}\,\mathrm{d}\mathbf{r}$$

yields the gauge-invariant phase difference γ_1 across the Josephson junction 1. In this way, we find

$$\gamma_2 - \gamma_1 = \mu_0 \lambda_\mathrm{L}^2 \left(\int_{1'}^{2'} \mathbf{j}_\mathrm{s}\,\mathrm{d}\mathbf{r} + \int_2^1 \mathbf{j}_\mathrm{s}\,\mathrm{d}\mathbf{r} \right) + \frac{2\pi}{\Phi_0} \Phi \tag{1.57}$$

Similar to the case of a massive circular ring, the magnetic flux Φ is given by the sum of the applied flux Φ_a and the self-field of the circulating currents *J*: $\Phi = \Phi_\mathrm{a} + LJ$. The contributions of the current densities are proportional to the circulating current J and can be included in the term LJ.[20] Finally, we obtain the relation we had been looking for

$$\gamma_2 - \gamma_1 = \frac{2\pi}{\Phi_0} \Phi = \frac{2\pi}{\Phi_0} (\Phi_\mathrm{a} + LJ) \tag{1.58}$$

20) Therefore, the inductivity of the ring is slightly increased. This contribution is referred to as "kinetic inductance" L_kin, which must be added to the inductance L given by the geometry. Hence, we have $L_\mathrm{tot} = L + L_\mathrm{kin}$. However, since mostly the contribution L_kin is very small, we will not distinguish any further between L_tot and L.

From Eqs. (1.53a), (1.53b) and (1.58), we can calculate the maximum supercurrent along the ring as a function of the applied magnetic field or of the flux.

Let us start by assuming that we can neglect the contribution of the term LJ to the magnetic flux. The circulating current J clearly cannot become larger than the critical current I_c of the Josephson junctions. Hence, the flux generated by the term LJ is smaller than LI_c. We assume also that this flux is much smaller than half a flux quantum, yielding the condition $2LI_c/\Phi_0 \ll 1$. The quantity $2LI_c/\Phi_0$ is referred to as the *inductance parameter* β_L,

$$\beta_L = \frac{2LI_c}{\Phi_0} \tag{1.59}$$

If we neglect the magnetic flux generated by the circulating current, we have $\Phi = \Phi_a$. Using Eq. (1.58), we eliminate γ_2 from Eqs. (1.53a) and (1.53b). Then, by adding Eqs. (1.53a) and (1.53b), we obtain

$$I = I_c \left[\sin \gamma_1 + \sin \left(2\pi \frac{\Phi_a}{\Phi_0} + \gamma_1 \right) \right] \tag{1.60}$$

Now it is advantageous to use the variable $\delta = \gamma_1 + \pi(\Phi_a/\Phi_0)$ instead of γ_1. Then Eq. (1.60) can be changed into

$$I = I_c \left[\sin \left(\delta - \pi \frac{\Phi_a}{\Phi_0} \right) + \sin \left(\delta + \pi \frac{\Phi_a}{\Phi_0} \right) \right] \tag{1.61}$$

By using the trigonometric identity for the summation of sines, we obtain the expression

$$I = 2I_c \sin \delta \cos \left(\pi \frac{\Phi_a}{\Phi_0} \right) \tag{1.62}$$

If we specify the flux Φ_a and the current I, the variable δ will adjust itself such that Eq. (1.62) is satisfied. For increasing current, this is possible at most up to the point where sin δ becomes equal to $+1$ or -1, depending on the current direction and on the sign of the cosine factor. Hence, the maximum supercurrent that can flow through this circular structure is given by

$$I_{s,max} = 2I_c \left| \cos \left(\pi \frac{\Phi_a}{\Phi_0} \right) \right| \tag{1.63}$$

The quantity $I_{s,max}$ reaches a maximum if the flux corresponds to an integer multiple of a flux quantum. Then the cosine factor is equal to 1, and we obtain $I_{s,max} = 2I_c$. This is the maximum supercurrent that can be carried by the parallel configuration of the two Josephson junctions. In this case, we have sin $\gamma_1 =$ sin $\gamma_2 = 1$. In this case, the circulating current J, obtained as

$$J = \frac{I_c}{2}(\sin \gamma_1 - \sin \gamma_2) \tag{1.64}$$

by subtraction of Eqs. (1.53a) and (1.53b), vanishes. The current $I_{s,max}$ vanishes each time that Φ_a reaches the value $(n + 1/2)\,\Phi_0$ with $n = 0, \pm 1, \pm 2, \ldots$ Now the circulating current attains its maximum value, becoming equal to $+I_c$ or $-I_c$ depending on the value of n.

The maximum supercurrent flowing within the circular structure also oscillates periodically as a function of the applied magnetic field. Here, the period of the magnetic flux generated by the field is the magnetic flux quantum. This effect was first demonstrated experimentally by Mercereau and coworkers [46]. It is the analogy of the diffraction of light by a double slit, and it represents the foundation of the application of such circular structures as a superconducting quantum interferometer (SQUID). We note that SQUIDs can measure an applied magnetic field continuously.

SQUIDs will be discussed in detail in Section 7.6.4. However, at this stage, we point out already that SQUIDs can resolve changes of the magnetic flux down to about $10^{-6}\Phi_0$. If the area of the SQUID is about 1 mm^2, then this corresponds to field changes ΔB of about $10^{-6}\Phi_0/\text{mm}^2 = 10^{-15}$ T, which can be detected with a SQUID.

This value is smaller than the Earth's magnetic field by 11 orders of magnitude, and approximately corresponds to the magnetic fields generated at the surface of the skull by the electric currents within the human brain. SQUIDs belong to the group of most sensitive detectors by far. Since the measurement of many physical quantities can be transformed into a magnetic field or flux measurement, SQUIDs find very wide applications.

Again, we can briefly discuss the analogy with the Sagnac interferometer. If in a constant external magnetic field the SQUID is rotating around an axis perpendicular to the area of the ring, a phase shift of $(2m/\hbar)2\pi R^2\Omega = 4\pi^2R^2(2m/h)\Omega$ results in the interferometer. Here, Ω is the angular velocity and $2m$ is the mass of a Cooper pair. We have assumed a circular SQUID with radius R. Hence, $I_{\text{s,max}}$ oscillates with a period depending on the ratio m/h. Already by 1950, Fritz London had pointed out the equivalence of a rotating superconductor and an externally applied magnetic field [47]. A similar rotational effect can also be observed with other coherent matter waves, for instance, with superfluid helium [48]. However, since the mass of helium atoms is much larger than that of Cooper pairs, for helium the sensitivity against rotation is much larger than for SQUIDs.

Next, we discuss briefly the approximations leading us to Eq. (1.63). We had assumed that the critical currents I_c of both Josephson junctions are identical. Without this assumption, we would find that $I_{\text{s,max}}$ varies between $I_{c1} + I_{c2}$ and $|I_{c1} - I_{c2}|$, where again the period is one flux quantum. So compared to Eq. (1.63), there is no qualitative change. Furthermore, the period of the oscillation remains unchanged if the finite inductance is taken into account. As before, the maximum value $I_{\text{s,max}}$ is again given by $I_{c1} + I_{c2}$. However, the minimum value of $I_{\text{s,max}}(\Phi)$ more and more approaches the maximum value. In Figure 1.26, we show this effect for three different values of the inductance parameter β_L.

For large values of the inductance parameter β_L, the relative modulation amplitude decreases proportional to $1/\beta_L$. In order to see this, we must remember that for a massive superconducting ring, a shielding current with a maximum value of $J = \Phi_0/2L$ was sufficient to supplement the applied flux until it reached the next integer value of Φ_0. If we apply this principle to the SQUID, the

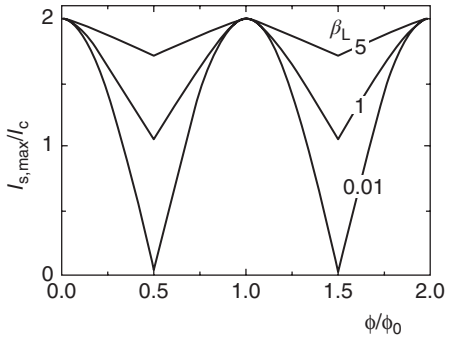

Figure 1.26 Modulation of the maximum supercurrent of a superconducting quantum interferometer as a function of the magnetic flux through the ring. The curves are shown for three different values of the inductance parameter β_L.

circulating current must not exceed the value $\Phi_0/2L$. For large values of the inductance, this circulating current is smaller than I_c, and $I_{s,max}$ is reduced to the value $2(I_c - J)$. Therefore, we obtain a relative modulation amplitude of $[2I_c - 2(I_c - J)]/2I_c = J/I_c = \Phi_0/(2LI_c) = 1/\beta_L$. Hence, the effect of the quantum interference decreases with increasing inductance.

If we include thermal fluctuation effects, one can show that the optimum sensitivity of SQUIDs against flux changes is reached for $\beta_L = 1$. However, for a given value of the critical current, this also limits the area of the SQUID ring, since the inductance increases with increasing circumference of the ring. Hence, on the one hand, one desires an area as large as possible in order to achieve a large change of flux with a small change of the magnetic field. On the other hand, this area cannot be too large, because otherwise the inductance would become too large. This conflict has resulted in a number of highly special SQUID geometries, which deviate strongly from the simple ring structure shown in Figure 1.25. We will discuss these geometries in Section 7.6.4.

Finally, we turn to the effects resulting from the finite size of the Josephson junctions. We will see that also the critical current of the junctions depends on the magnetic field or on the magnetic flux through the junction, in analogy to the diffraction of light at a double slit.

Let us look at the geometry of a spatially extended Josephson junction shown schematically in Figure 1.27. We assume that this junction is penetrated by a magnetic field along the z-direction parallel to the barrier layer. We look for an equation describing the dependence of the gauge-invariant phase difference γ on the applied magnetic field. For the superconducting ring of Figure 1.25, we saw that the difference $\gamma_2 - \gamma_1$ of the two phases of the Josephson junctions, assumed to represent point junctions, is proportional to the magnetic flux enclosed between these junctions.

In analogy to the earlier derivation of the relevant equations, we look at the path along which we want to integrate the wave vector of the superconducting wave function. In Figure 1.27, this path is shown as the dotted line. Along the x-axis

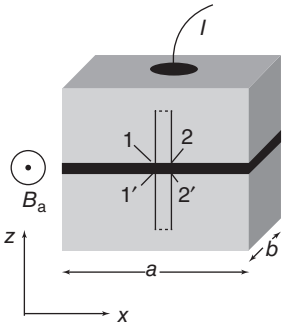

Figure 1.27 Geometry of the spatially extended Josephson junction.

the path extends from point x to point $x + \mathrm{d}x$, where $\mathrm{d}x$ denotes an infinitesimally small distance. Along the y-direction the path extends deeply into the interior of both superconductors, for which we assume that they are much thicker than the London penetration depth. In analogy to Eq. (1.57), we find

$$\gamma(x + \mathrm{d}x) - \gamma(x) = \mu_0 \lambda_\mathrm{L}^2 \left(\int_{1'}^{2'} \mathbf{j}_\mathrm{s}\, \mathrm{d}\mathbf{r} + \int_{2}^{1} \mathbf{j}_\mathrm{s}\, \mathrm{d}\mathbf{r} \right) + \frac{2\pi}{\Phi_0} \Phi_1 \tag{1.65}$$

Here, Φ_I denotes the total flux enclosed by the integration path. Beyond a layer of depth λ_L, the shielding currents in the superconducting electrodes are exponentially small. Therefore, we can neglect the two integrals taken over the supercurrent densities. Furthermore, we assume that the supercurrents and the magnetic fields vary along the x-direction, but not along the y-direction. Then we write for the magnetic flux

$$\Phi_1 = B\, t_\mathrm{eff}\, \mathrm{d}x \tag{1.66}$$

We find the "effective thickness" t_eff by integrating the magnetic field along the z-direction. Since the magnetic field decays exponentially in the two superconductors within a characteristic length λ_L, this integration yields

$$t_\mathrm{eff} = \lambda_{\mathrm{L},1} + \lambda_{\mathrm{L},2} + t_\mathrm{b} \tag{1.67}$$

Here, $\lambda_{\mathrm{L},1}$ and $\lambda_{\mathrm{L},2}$ are the London penetration depths in the two superconductors, respectively. They do not have to be identical. The thickness of the barrier layer is denoted by t_b. In general, it is much smaller than $\lambda_{\mathrm{L},1}$ and $\lambda_{\mathrm{L},2}$. Hence, mostly it can be neglected.

With these assumptions and notations, from Eq. (1.65) we obtain the differential equation

$$\gamma' \equiv \frac{\mathrm{d}\gamma}{\mathrm{d}x} = \frac{2\pi}{\Phi_0} B t_\mathrm{eff} \tag{1.68}$$

yielding the connection we had been looking for.

Furthermore, we assume that we can neglect the self-field generated by the Josephson currents. This assumption represents a condition about the spatial extension of the junction along the x and y directions. In Section 6.4, we will see

that it is necessary that the lengths a and b of the edges of the junction do not exceed the so-called Josephson penetration depth

$$\lambda_J = \sqrt{\frac{\Phi_0}{2\pi\mu_0 j_c l_{eff}}} \tag{1.69}$$

Here, j_c is the critical supercurrent density, assumed to be spatially homogeneous, and the length l_{eff} is equal to t_{eff} if the superconducting electrodes are much thicker than λ_L, as we had assumed. Typically, the Josephson penetration depth is a few micrometers. However, it can also increase up to the millimeter scale if the critical supercurrent density is very small.

With the assumptions indicated earlier, the magnetic field B is equal to the externally applied field B_a. Then we can integrate Eq. (1.68) and obtain

$$\gamma(x) = \gamma(0) + \frac{2\pi}{\Phi_0} B_a t_{eff} x \tag{1.70}$$

The gauge-invariant phase difference is seen to increase linearly with the x-coordinate. Inserting this function $\gamma(x)$ into the first Josephson equation, we obtain for the spatial dependence of the supercurrent density across the barrier layer

$$j_s(x) = j_c \sin\left[\gamma(0) + \frac{2\pi}{\Phi_0} B_a t_{eff} x\right] \tag{1.71}$$

We see that the supercurrent density oscillates along the x-coordinate, that is, perpendicular to the applied field. Here, the wavelength of the oscillation is determined by the applied magnetic field.

Now we want to calculate the maximum Josephson current that can flow across the Josephson junction. For this we integrate Eq. (1.71) over the area of the junction:

$$I_s = \int_0^b dy \int_0^a dx\, j_c \sin\left[\gamma(0) + \frac{2\pi}{\Phi_0} B_a t_{eff} x\right] \tag{1.72a}$$

Next we assume that the critical supercurrent density j_c is spatially homogeneous, that is, it is independent of x and y. Then the integration yields

$$I_s = j_c b \int_0^a dx \sin\left[\gamma(0) + \frac{2\pi}{\Phi_0} B_a t_{eff} x\right] = -j_c b \frac{\cos\left[\gamma(0) + \frac{2\pi}{\Phi_0} B_a t_{eff} x\right]}{\frac{2\pi}{\Phi_0} B_a t_{eff}}\Bigg|_0^a \tag{1.72b}$$

Inserting the integration limits, we obtain

$$I_s = j_c b \frac{\cos\gamma(0) - \cos\left[\gamma(0) + \frac{2\pi}{\Phi_0} B_a t_{eff} a\right]}{\frac{2\pi}{\Phi_0} B_a t_{eff}} \tag{1.72c}$$

With the variable $\delta = \gamma(0) + (\pi/\Phi_0)\, B_a t_{eff} a$ and using the relation $\cos(\alpha \pm \beta) = \cos\alpha \cos\beta \mp \sin\alpha \sin\beta$, finally we find

$$I_s = j_c ab \;\; \sin\delta \;\; \frac{\sin\left[\frac{\pi}{\Phi_0} B_a t_{eff} a\right]}{\frac{\pi}{\Phi_0} B_a t_{eff} a} \tag{1.72d}$$

Similar to Eq. (1.62), for a given current I and magnetic field B_a, the quantity δ will adjust itself in such a way that Eq. (1.72d) will be satisfied. This is possible up to the value for which $\sin\delta = \pm 1$, and finally we obtain the magnetic field dependence of the critical current of the Josephson junction

$$I_c(\Phi_J) = I_c(0)\left|\frac{\sin\left[\pi\frac{\Phi_J}{\Phi_0}\right]}{\pi\frac{\Phi_J}{\Phi_0}}\right| \tag{1.73}$$

where $\Phi_J = B_a t_{eff} a$ and $I_c(0) = j_c ab$. The quantity Φ_J corresponds to the magnetic flux penetrating the Josephson junction.

The function 1.73 is shown in Figure 1.28a. In analogy to the diffraction of light by a slit, it is referred to as a *Fraunhofer pattern*. In Figure 1.28b, we see the measured dependence $I_c(B_a)$ for a Sn–SnO–Sn tunnel junction. With a value of the London penetration depth of 30 nm, one obtains for t_{eff} a value of about 60 nm. The width of the junction was 250 µm. Hence, we expect zero values of the critical current within a distance $\Delta B_a = \Phi_0/(at_{eff}) \approx 1.4\,\text{G}$. This agrees well with the experimental result $\Delta B_a = 1.25\,\text{G}$.

If the critical current density j_c had been inhomogeneous, that is, depending upon the spatial coordinates x and y, the function $I_c(B_a)$ would have deviated strongly from the form of the Fraunhofer pattern. Therefore, the measurement of $I_c(B_a)$ often serves as a simple test of the homogeneity of the barrier layer.

What about the physics behind the Fraunhofer pattern? For light diffraction by a slit, minima in the interference stripes appear at locations where the waves passing through the slit interfere destructively with each other. According to Eq. (1.70), in the Josephson junction the magnetic field causes an increase in the gauge-invariant phase difference along the barrier, and the supercurrent density spatially

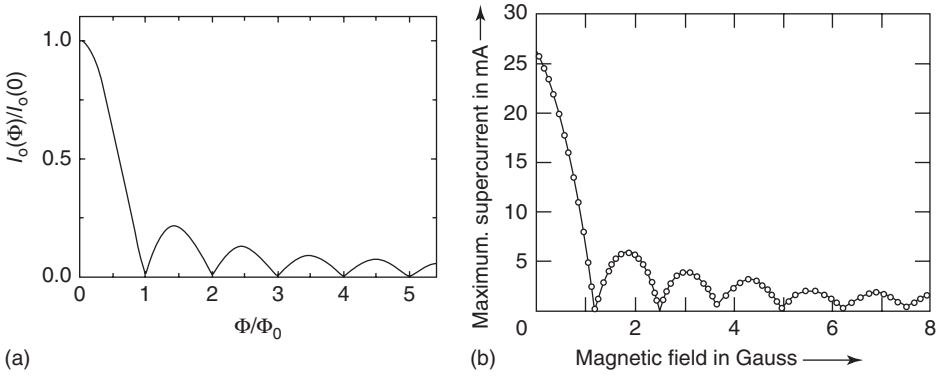

Figure 1.28 Dependence of the maximum Josephson current on the magnetic field parallel to the barrier layer. (a) Theoretical curve according to Eq. (1.73). (b) Measured data for a Sn–SnO–Sn tunnel junction ($1\,\text{G} = 10^{-4}\,\text{T}$). .(From [49].)

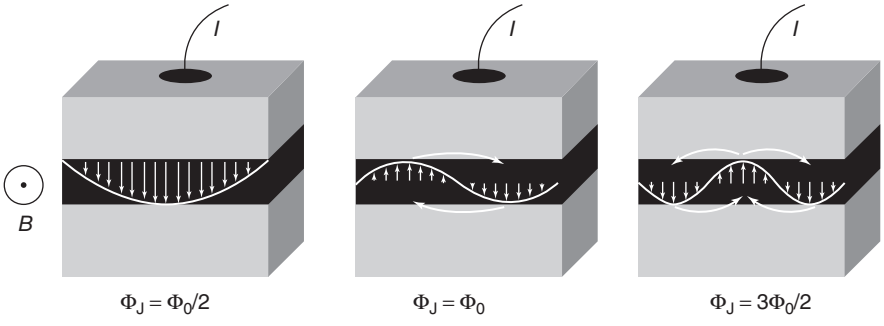

Figure 1.29 Variation of the Josephson supercurrent density for three different values of the magnetic flux penetrating through the Josephson junction.

oscillates in the x-directions.[21] At the zero values of $I_c(\Phi)$, the wavelength of these oscillations is an integer fraction of the width a of the junction. Hence, equal amounts of the supercurrent flow across the barrier in both directions, and the integral over the supercurrent density is zero, independent of the value of the initial phase $\gamma(0)$ in Eq. (1.70). However, away from the zero values, the wavelength of the supercurrent density is incommensurable with the width of the junction. In this case the supercurrent can attain a finite value, which is adjustable up to a certain maximum value by means of the phase shift $\gamma(0)$. This maximum value becomes smaller for smaller wavelengths of the oscillations of the supercurrent density, since the supercurrents more and more average to zero over an increasing number of periods.

In Figure 1.29, we show this effect for three different spatial distributions of the current density at values of the flux $\Phi_0/2$, Φ_0, and $3\Phi_0/2$. For the values $\Phi_0/2$ and $3\Phi_0/2$, the phase $\gamma(0)$ is chosen such that the supercurrent across the junction reaches a maximum value. For the value Φ_0 the supercurrent across the junction is always zero, independent of $\gamma(0)$. Furthermore, we note that the fraction of the Josephson current not flowing in the forward direction across the junction must flow in a closed loop within the superconducting electrodes. In Figure 1.29, this is indicated by the "horizontal" arrows.

What happens, finally, if the self-field generated by the Josephson current is taken into account? If the effect of the self-field is small, such that the magnetic flux generated by this field is much smaller than Φ_0, the correction of the applied field remains small. However, if the magnetic flux generated by the supercurrents circulating across the barrier approaches the value Φ_0, vortices can appear with their axis located within the barrier layer. These vortices are also referred to as *Josephson flux quanta* or *fluxons*. They display many interesting properties, which we will discuss in more detail in Section 6.4. In particular, based on moving Josephson vortices, high-frequency oscillators can be built that are utilized in the application of Josephson junctions for the detection of microwaves (see Section 7.6.3).

21) This current distribution can be imaged by means of low-temperature scanning electron microscopy. Details can be found in the literature [50].

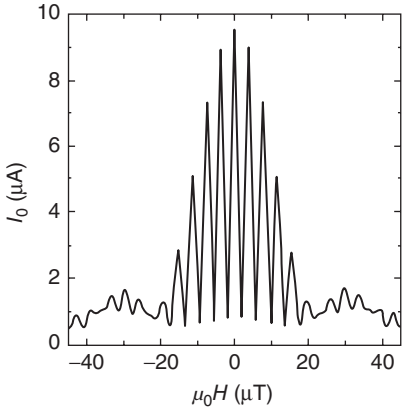

Figure 1.30 Magnetic field dependence of the maximum supercurrent of a SQUID structure made of $YBa_2Cu_3O_7$. The two Josephson junctions are 9 μm wide, such that the I_c modulation of the individual junctions appears as the envelope of the SQUID oscillations [51]. (© 2000 AIP.)

Let us go back to the circular structure of Figure 1.25. If here the finite extension of both Josephson junctions is taken into account, the magnetic field dependence of their critical currents and the periodic modulation of the maximum supercurrent that can pass through the circular structure are superimposed on each other. Formally, we can account for this, for example, by replacing I_c in Eq. (1.62) by Eq. (1.72d). For a typical SQUID, the area at_{eff} of both Josephson junctions is smaller than that of the SQUID itself by several orders of magnitude. The maximum supercurrent oscillates on a field scale of a few microtesla, whereas the critical current of the Josephson junctions decreases appreciably only at fields of about 1 m T. So sometimes one can observe thousands of oscillations with nearly the same maximum amplitude $I_{c1} + I_{c2}$. However, in some cases, geometric structures have been investigated in which the SQUID area and the dimension of the Josephson junctions were similar. In Figure 1.30, we show an example obtained with a circular structure made of $YBa_2Cu_3O_7$, for which the area at_{eff} of the Josephson junctions was just barely by a factor 10 smaller than the ring area [51]. Here, we can clearly see the superposition of the SQUID modulation and of the Fraunhofer pattern.

At the end of this chapter, we now turn to the question: In which form can similar interference phenomena be observed also for individual electrons? We imagine that the matter wave describing an individual electron is split into two spatially separated coherent parts, which subsequently are caused to interfere with each other. If the area enclosed by the two partial beams is penetrated by the flux Φ, we expect a phase difference between the two partial beams. For a flux of h/e, that is, for twice the value observed in superconductors, the phase difference will be 2π.

Such an experiment was carried out in 1962 by Möllenstedt and coworkers using electron waves in a vacuum [51]. By means of a very thin, negatively charged wire (a so-called biprism), they split an electron beam into two partial beams, which they guided around a tiny coil (diameter about 20 μm) to the other side. By using additional biprisms, subsequently both beams were superimposed, yielding a system of interference stripes. Indeed, they obtained the well-known interference

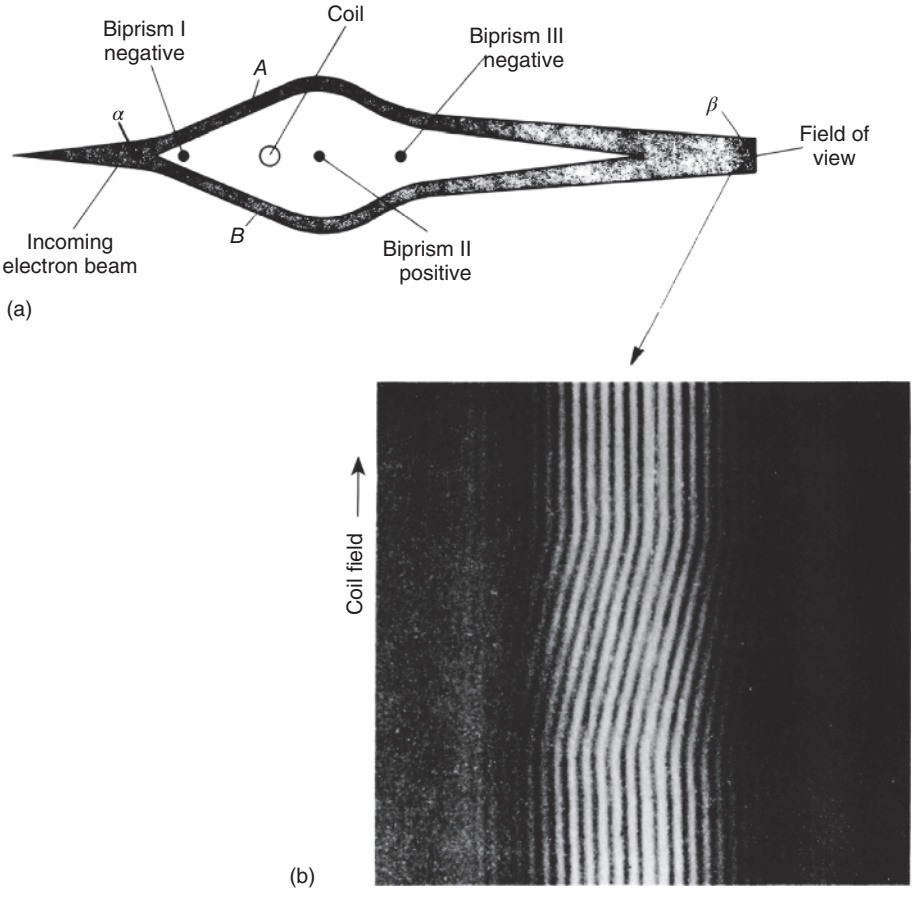

Figure 1.31 Phase change of electron waves caused by a vector potential. (a) Beam geometry. (b) Interference pattern during a change of the magnetic field. The biprisms are quartz threads covered by a metal. The coil with 20 μm diameter was fabricated from tungsten wire. (From [52].)

pattern of the double slit. Next, the system of interference stripes was studied for different magnetic fields in the coil. A change of the magnetic field affected a shift of the system of stripes, displaying the expected phase shift of 2π for a flux change of h/e. In Figure 1.31, we present a schematic of the experiment (a) and a picture of the system of stripes (b). During the change of the magnetic field, the recording film was moved parallel to the system of stripes. The shift in the system of stripes can clearly be seen. In Figure 1.31b for the total field change, the shift amounts to about three complete periods. Hence, in this experiment, the phase difference between the partial beams was changed by the magnetic field by about $3 \times 2\pi$.

The special feature of this experiment is the fact that the magnetic field was very carefully restricted to the interior of the coil. In this experiment, the field lines of

the return flux were concentrated into a yoke made of a magnetic material and placed outside the loop area of the electron beams. The shift of the interference pattern was observed, although no Lorentz force acted on the electrons. The only forces were the constant electrostatic forces originating from the biprisms. Hence, an effect appears that cannot be explained within a classical particle concept. The interference pattern changed as a function of the magnetic flux enclosed between the two particle beams, without additional forces acting on the electron trajectory. This non-classical effect was predicted already in 1959 by Aharonov and Bohm [53]. Subsequently, its discussion was highly controversial. However, the prediction of Aharonov and Bohm could be confirmed by means of ring-shaped magnets covered with a superconducting overlay, such that the magnetic field was completely restricted to the interior of the magnets [14].

Based on this principle of electron holography, also the flux lines shown in Figure 1.10d were imaged. In this experiment, quantum mechanics appears twofold: on the one hand, the wave nature of the electrons was utilized for imaging; on the other, it was the quantized magnetic flux of a vortex that was detected in the superconductor.

The observation of flux quantization and of quantum interference in Josephson junctions and in SQUID rings has clearly shown that the appearance of a coherent matter wave represents the key property of the superconducting state. For the amount of charge of the superconducting charge carriers, the value $2e$ has always been found. In Chapter 3, we will describe how this Cooper pairing is accomplished. However, first we will turn to the different superconducting materials.

References

1. H. Kamerlingh-Onnes: *Commun. Leiden* **140b, c** and **141b** (1914).
2. Kamerlingh-Onnes, H. (1924) Reports and Communication 4. International Cryogenic Congress, London, p. 175; H. Kamerlingh-Onnes, W. Tuyn: *Commun. Leiden* **198** (1929) .
3. D. J. Quinn, W. B. Ittner: *J. Appl. Phys.* **33**, 748 (1962).
4. H. Kamerlingh-Onnes: *Commun. Leiden* **50a** (1924).
5. C. J. Gorter, H. Casimir: *Physica* **1**, 306 (1934).
6. W. Meißner, R. Ochsenfeld: *Naturwissenschaften* **21**, 787 (1933).
7. Geim, A. (1998) Physics Today, September 1998, p. 36.
8. D. Cribier, B. Jacrot, L. Madhav Rao, B. Farnoux: *Phys. Lett.* **9**, 106 (1964); see also: "*Progress Low Temperature Physics*", Vol. **5**, C. J. Gorter (ed.), North Holland Publishing Company, Amsterdam, p. 161 (1967).
9. J. Schelten, H. Ullmaier, W. Schmatz: *Phys. Status Solidi* **48**, 619 (1971).
10. U. Essmann, H. Träuble: *Phys. Lett.* **24 A**, 526 (1967) and *J. Sci. Instrum.* **43**, 344 (1966).
11. P. E. Goa, H. Hauglin, M. Baziljevich, E. Il'yashenko, P. L. Gammel, T. H. Johansen: *Supercond. Sci. Technol.* **14**, 729 (2001).
12. T. Matsuda, S. Hasegawa, M. Igarashi, T. Kobayashi, M. Naito, H. Kajiyama, J. Endo, N. Osakabe, A. Tonomura, R. Aoki: *Phys. Rev. Lett.* **62**, 2519 (1989)
13. R. Straub, S. Keil, R. Kleiner, D. Koelle: *Appl. Phys. Lett.* **78**, 3645 (2001)
14. A. Tonomura: "*Electron Holography*", Springer Series in Optical Sciences Vol. **70** (1998).
15. R. Gross, D. Koelle: *Rep. Prog. Phys.* **57**, 651 (1994).

16. A. de Lozanne: *Supercond. Sci. Technol.* **12**, p. R43 (1999).
17. A. Oral, J. C. Barnard, S. J. Bending, I. I. Kaya, S. Ooi, T. Tamegai, M. Henini: *Phys. Rev. Lett.* **80**, 3610 (1998).
18. J. R. Kirtley, M. B. Ketchen, K. G. Stawiasz, J. Z. Sun, W. J. Gallagher, S. H. Blanton, S. J. Wind: *Appl. Phys. Lett.* **66**, 1138(1995); R. C. Black, F. C. Wellstood, E. Dantsker, A. H. Miklich, D. Koelle, F. Ludwig, J. Clarke: *Appl. Phys. Lett.* **66**, 1267 (1995).
19. H. F. Hess, R. B. Robinson, J. V. Waszczak: *Phys. Rev. Lett.* **64**, 2711 (1990).
20. L. Schultz, G. Krabbes, G. Fuchs, W. Pfeiffer, K.-H. Müller: *Z. Metallk.* **93**, 1057 (2002).
21. F. London: "*Superfluids*", Vol. **1**, John Wiley & Sons, Inc., New York, p. 152 (1950).
22. R. Doll, M. Näbauer: *Phys. Rev. Lett.* **7**, 51 (1961).
23. B. S. Deaver Jr., W. M. Fairbank: *Phys. Rev. Lett.* **7**, 43 (1961).
24. F. London, H. London: *Z. Phys.* **96**, 359 (1935); F. London: "*Une Conception Nouvelle de La Supraconductivite*", Hermann, Cie, Paris (1937).
25. J. M. Lock: *Proc. R. Soc. London, Ser. A* **208** 391 (1951).
26. T. J. Jackson, T. M. Risemann, E. M. Forgan, H. Glückler, T. Prokscha, E. Morenzoni, M. Pleines, Ch. Niedermayer, G. Schatz, H. Luetkens, J. Litterst: *Phys. Rev. Lett.* **84**, 4958 (2000).
27. A. B. Pippard: *Proc. R. Soc. London, Ser. A* **203**, 210 (1950).
28. J. S. Langer, V. Ambegaokar: *Phys. Rev.* **164**, 498 (1967).
29. D. E. McCumber, B. I. Halperin: *Phys. Rev. B* **1**, 1054 (1970).
30. J. E. Lukens, R. J. Warburton, W. W. Webb: *Phys. Rev. Lett.* **25**, 1180 (1970).
31. R. S. Newbower, M. R. Beasley, M. Tinkham: *Phys. Rev. B* **5**, 864 (1972).
32. B. D. Josephson: *Phys. Lett.* **1**, 251 (1962).
33. R.P. Feynman, R.B. Leighton, M. Sands: "*Feynman Lectures on Physics*", Vol. **3**, Addison-Wesley Publishing Company, New York (1965).
34. L. D. Landau, E. M. Lifschitz: "*Lehrbuch der Theoretischen Physik*", Vol. **9**, Akademie-Verlag, Berlin, 1980.
35. R. Gross: In "*Interfaces in High-T_c Superconducting Systems*", S. L. Shinde, D. A. Rudman (eds.), Springer, New York, p. 176 (1994).
36. H. Hilgenkamp, J. Mannhart: *Rev. Mod. Phys.* **74** (2002).
37. R. Kleiner, F. Steinmeyer, G. Kunkel, P. Müller: *Phys. Rev. Lett.* **68**, 2394 (1992).
38. J. S. Tsai, A. K. Jain, J. E. Lukens: *Phys. Rev. Lett.* **51**, 316 (1983).
39. D. G. McDonald: *Science* **247**, 177 (1990).
40. S. Shapiro: *Phys. Rev. Lett.* **11**, 80 (1963).
41. I. Giaever: *Phys. Rev. Lett.* **14**, 904 (1965).
42. A. H. Dayem, R. J. Martin: *Phys. Rev. Lett.* **8**, 246 (1962).
43. D. N. Langenberg, D. J. Scalapino, B. N. Taylor, R. E. Eck: *Phys. Rev. Lett.* **15**, 294 (1965).
44. I. K. Yanson, V. M. Svistunov, I. M. Dmitrenko: *Zh. Eksperim. Teor. Fiz.* **48**, 976 (1965); I. K. Yanson, V. M. Svistunov, I. M. Dmitrenko: *Sov. Phys. JETP* **21**, 650 (1966).
45. D. N. Langenberg, W. H. Parker, B. N. Taylor: *Phys. Rev.* **150**, 186 (1966); D. N. Langenberg, W. H. Parker, B. N. Taylor: *Phys. Rev. Lett.* **18**, 287 (1967).
46. R. C. Jaklevic, J. Lambe, J. E. Mercereau, A. H. Silver: *Phys. Rev.* **140 A**, 1628 (1965).
47. F. London: "*Superfluids, Macroscopic Theory of Superconductivity*", Vol. **1**, John Wiley & Sons, Inc., New York (1950).
48. R. E. Packard, S. Vitale: *Phys. Rev. B* **46**, 3540 (1992); O. Avenel, P. Hakonen, E. Varoquaux, *Phys. Rev. Lett.* **78**, 3602 (1997); K. Schwab, N. Bruckner, R. E. Packard: *Nature* **386**, 585 (1997).
49. D. N. Langenberg, D. J. Scalapino, B. N. Taylor: *Proc. IEEE* **54**, 560 (1966).
50. C. Gürlich, S. Scharinger, M. Weides, H. Kohlstedt, R. G. MInts, E. Goldobin, D. Koelle, R. Kleiner: *Phys. Rev. B* **81**, 094502 (2010).
51. R. R. Schulz, B. Chesca, B. Goetz, C. W. Schneider, A. Schmehl, H. Bielefeldt, H. Hilgenkamp, J. Mannhart, C. C. Tsuei: *Appl. Phys. Lett.* **76**, 912 (2000).

52. G. Möllenstedt, W. Bayh: *Phys. Bl.* **18**, 299 (1962); G. Möllenstedt, W. Bayh: *Naturwissenschaften* **49**, 81 (1962).
53. Y. Aharonov, D. Bohm: *Phys. Rev.* **115**, 485 (1959).
54. L. Ozyuzer, A. E. Koshelev, C. Kurter, N. Gopalsami, Q. Li, M. Tachiki, K. Kadowaki, T. Yamamoto, H. Minami, H. Yamaguchi, T. Tachiki, K. E. Gray, W. K. Kwok, U. Welp: *Science* **318**, 1291 (2007).
55. H. B. Wang, S. Guénon, B. Gross, J. Yuan, Z. G. Jiang, Y. Y. Zhong, M. Grünzweig, A. Iishi, P. H. Wu, T. Hatano, D. Koelle, R. Kleiner: *Phys. Rev. Lett.* **105**, 057002 (2010).